JCB Journal of Cell Biology

ARTICLE

Occluding junctions as novel regulators of tissue mechanics during wound repair

Lara Carvalho[1], Pedro Patricio[1,2,3], Susana Ponte[1], Carl-Philipp Heisenberg[4], Luis Almeida[5], André S. Nunes[3,6], Nuno A.M. Araújo[3,6], and Antonio Jacinto[1,7]

In epithelial tissues, cells tightly connect to each other through cell–cell junctions, but they also present the remarkable capacity of reorganizing themselves without compromising tissue integrity. Upon injury, simple epithelia efficiently resolve small lesions through the action of actin cytoskeleton contractile structures at the wound edge and cellular rearrangements. However, the underlying mechanisms and how they cooperate are still poorly understood. In this study, we combine live imaging and theoretical modeling to reveal a novel and indispensable role for occluding junctions (OJs) in this process. We demonstrate that OJ loss of function leads to defects in wound-closure dynamics: instead of contracting, wounds dramatically increase their area. OJ mutants exhibit phenotypes in cell shape, cellular rearrangements, and mechanical properties as well as in actin cytoskeleton dynamics at the wound edge. We propose that OJs are essential for wound closure by impacting on epithelial mechanics at the tissue level, which in turn is crucial for correct regulation of the cellular events occurring at the wound edge.

Introduction

A unifying feature of metazoans is the evolution of a physical barrier between the external environment and the different compartments of the body. Epithelia are the masters in this fundamental function. Various types of intercellular junctions are responsible for establishing cell–cell contacts, polarity, and a permeability barrier in epithelial tissues. Adherens junctions (AJs) bind epithelial cells together and maintain the mechanical integrity of epithelia (Harris and Tepass, 2010). In turn, occluding junctions (OJs) control the paracellular transport of molecules across the epithelium and separate the apical and the basolateral membrane compartments. OJs are present in virtually all metazoans, although their structure varies in different organisms. Two main types of OJs have been characterized: tight junctions (TJs), present in vertebrates, and septate junctions (SJs), typical of invertebrates (Shen, 2012; Jonusaite et al., 2016). TJs and SJs show differences in their ultrastructure, molecular composition, and subcellular localization, but they share key components, namely proteins of the claudin, membrane guanylate cyclase kinase, and immunoglobulin families. Additionally, SJs present a similar ultrastructure and share many molecular components (e.g., Na^+/K^+ ATPase, neurexins, and band 4.1 protein) with vertebrate paranodal junctions, which connect myelinated glial cells to axons and segregate the nodes of Ranvier from adjacent myelinated domains (Harden et al., 2016).

Several studies using the fruit fly *Drosophila melanogaster* have identified >20 proteins localized at the SJ, all obligatory for epithelial development and conserved across Bilateria (Jonusaite et al., 2016). By the end of embryogenesis, SJ components form a large, stable, and functional molecular complex at the apical region of epithelial cells. Notably, the loss of function of a single component is enough to destabilize the complex and impair SJ function (Laval et al., 2008; Oshima and Fehon, 2011).

Although the establishment of the paracellular barrier is the canonical function of OJs, recent studies suggest they also play a role in epithelial remodeling and morphogenesis independently of their barrier function. However, the underlying mechanisms are still unknown (Wu and Beitel, 2004; Balda and Matter, 2016; Hall and Ward, 2016). In vertebrates, TJs can influence different cellular complexes such as the actin cytoskeleton and Rho-GTPase signaling. It is well known that actin can regulate mechano-

[1]Chronic Diseases Research Center, NOVA Medical School/Faculdade de Ciências Médicas, Universidade NOVA de Lisboa, Lisbon, Portugal; [2]Instituto Superior de Engenharia de Lisboa, Instituto Politécnico de Lisboa, Lisbon, Portugal; [3]Centro de Física Teórica e Computacional, Universidade de Lisboa, Campo Grande, Lisbon, Portugal; [4]Institute of Science and Technology Austria, Klosterneuburg, Austria; [5]Centre National de la Recherche Scientifique/Sorbonne Université/Team Mamba, French Institute for Research in Computer Science and Automation Paris, Laboratoire Jacques-Louis Lions, BC187, Paris, France; [6]Departamento de Física, Faculdade de Ciências, Universidade de Lisboa, Campo Grande, Lisbon, Portugal; [7]The Discoveries Centre for Regenerative and Precision Medicine, Universidade NOVA de Lisboa, Lisbon, Portugal.

Correspondence to Antonio Jacinto: antonio.jacinto@nms.unl.pt; Lara Carvalho: lara.carvalho@nms.unl.pt.

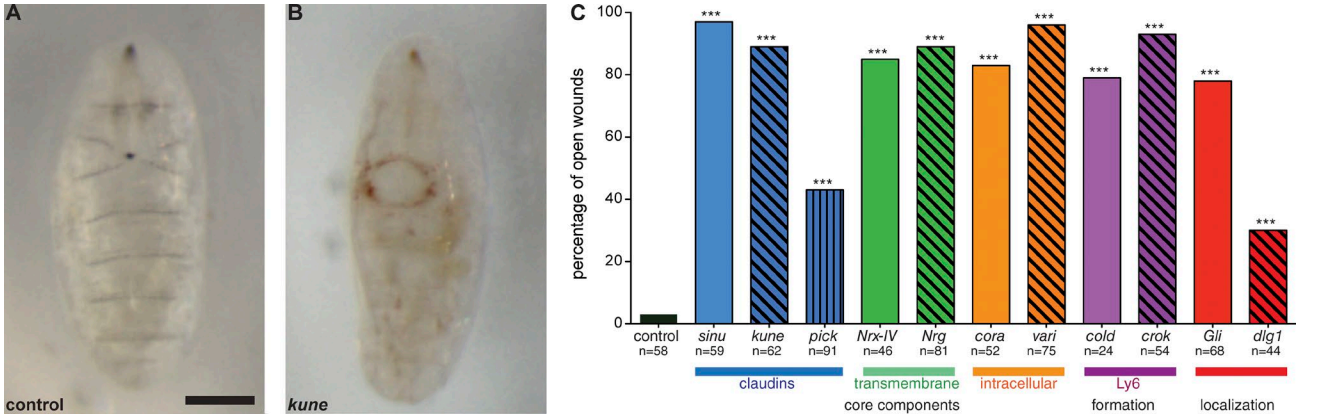

Figure 1. **Mutants for SJ-related proteins show wound-closure defects. (A and B)** WT embryo (A) and *kune* mutant embryo (B) 16 h after wounding. Bar, 100 µm. **(C)** Graph shows the percentage of open wounds 16 h after wounding in WT and SJ mutant embryos. Mutants for different types of SJ components were tested: claudin transmembrane proteins (blue), other transmembrane adhesion proteins (green), intracellular scaffolding proteins (orange), Ly6 family proteins that regulate SJ complex assembly (magenta), and proteins that regulate SJ localization (red). Fisher's exact test shows that all these SJ mutants have significantly higher percentages of open wounds when compared with controls. ***, $P < 0.0001$. See figure for the number of embryos for each genotype.

transduction by interacting with AJs. However, the link between OJs and the cytoskeleton as well as the potential role of these junctions in epithelial mechanics and morphogenesis remain largely unexplored (Sluysmans et al., 2017). Interestingly, in an unbiased genetic screen in *Drosophila*, the SJ-associated protein Coiled (Cold) has been found to be required for wound healing in the embryonic epidermis (Campos et al., 2010). Extensive work from several groups has shown that in simple epithelia of both vertebrates and invertebrates, wound closure initiates by cytoskeleton polarization in cells at the wound margin, leading to the accumulation of F-actin and nonmuscle myosin 2 at the boundary that faces the epithelial hole (Kiehart et al., 2000; Wood et al., 2002; Garcia-Fernandez et al., 2009; Zulueta-Coarasa and Fernandez-Gonzalez, 2017). This results in the formation of a contractile supracellular cable that pulls cells together, acting as a "purse string" to quickly close the gap. In *Drosophila*, AJs are required for the proper assembly of this so-called actomyosin cable and hence for successful wound healing (Abreu-Blanco et al., 2012; Carvalho et al., 2014; Hunter et al., 2015; Matsubayashi et al., 2015), but the contribution of SJs remains unknown.

These observations have motivated us to investigate the role of SJs in epithelial repair. In this study, we show that 11 SJ-related proteins are indispensable for efficient wound closure in the *Drosophila* embryonic epidermis. Mutants for SJ components develop a dysfunctional actomyosin cable at the wound margin and display impaired wound-closure dynamics. In addition, these mutants show defects in cellular shapes and rearrangements as well as in tissue mechanical properties, suggesting that SJs regulate the cohesion and the mechanical responses of the epidermis at the tissue level. Altogether, this work uncovers a novel role for OJs in the regulation of tissue mechanics during epithelial morphogenesis and repair.

Results

SJ core and associated proteins are required for wound healing

To investigate the role of SJs during wound healing, we determined whether mutants for the core components of SJs show a wound-closure phenotype using a previously described wounding assay (Campos et al., 2010). Briefly, we laser wounded the ventral epidermis of late-stage *Drosophila* embryos and scored them for open and closed wounds 16 h later (Fig. 1, A and B). Whereas only 3% of control embryos failed to close their wounds, mutants for seven SJ core components showed >80% of open wounds (Fig. 1 C). In addition, mutants for regulators of SJ assembly (Crooked) and localization (Gliotactin and Discs large [Dlg]; Oshima and Fehon, 2011) also showed a significant wound-closure phenotype (Fig. 1 C). These results show that SJs are essential for epithelial wound healing in *Drosophila* embryos.

SJ mutants show altered wound-closure dynamics

To understand the loss-of-function phenotype of SJ components during wound healing, we focused our analysis on the mutant *kune-kune* (*kune*), which showed a strong phenotype in our wounding assay (89% of unclosed wounds; Fig. 1 C). The protein Kune belongs to the claudin family, also essential components of vertebrate TJs (Nelson et al., 2010). We imaged live WT and *kune* mutant embryos expressing *Cherry::Moesin* to detect the F-actin cytoskeleton (Millard and Martin, 2008) and followed the formation and contraction of the actin cable at the wound edge upon laser wounding by spinning-disk confocal microscopy (Video 1). In the WT, this process occurred in a stereotypical manner as previously described (Fig. 2 A; Abreu-Blanco et al., 2012). In the first minutes after injury, cells at the wound edge began to accumulate actin at the boundary facing the hole, and ∼15–20 min later, an actin cable had assembled; the wound edge then contracted and eventually drove the hole to close. These wounds took on average 62 min to close completely (Fig. 2, D and F). In *kune* mutants, the dynamics of closure were dramatically impaired, and two phenotype strengths were noticed. *kune* embryos showing a mild phenotype (*kune* "mild" mutants) formed an actin cable at the wound edge and initiated contraction, but closure took much longer than in the WT (Fig. 2, B, D, and F); these embryos took on average 160 min to fully close their wounds. *kune* "strong" mutants exhibited a more severe phenotype: in the first 20 min after wounding, wound edge cells also assembled an actin cable and

started contracting, slightly decreasing the area of the hole, but at a significantly slower rate than control embryos (closure rate of controls = 28 μm²/min; closure rate of *kune* strong mutants = 8 μm²/min). 20–40 min after injury, the wounds stopped decreasing size and gradually expanded, in some cases reaching >3× the initial wound size (Fig. 2, C and F); at the same time, the actin cable seemed to progressively decrease in intensity. Strikingly, 2–3 h after wounding, *kune* strong mutants restarted contracting and either eventually reached closure (average = 285 min; *n* = 3 out of 8 embryos) or failed to close the wound until the end of the time-lapse imaging (maximum 315 min after wounding; *n* = 5 out of 8 embryos; Fig. 2 D). Interestingly, the average initial wound area was larger in *kune* strong mutants than in controls and *kune* mild embryos (Fig. 2 E), suggesting that the observed wound-closure phenotypes are associated with defects in the epithelium before injury. To confirm whether there is a correlation between the wound size and the phenotype strength in *kune* mutants, we divided wounds in two groups according to their initial area: small (initial wound area = 468–1,100 μm²) and large (initial wound area = 1,101–1,820 μm²). Indeed, large wounds closed significantly later than small wounds in *kune* mutants (Fig. 2 G). In addition, small wounds were predominant in the mild phenotype cohort, whereas large wounds were more associated with the strong phenotype (Fig. 2 H). Similar results were obtained for the mutant *sinuous* (*sinu*), another SJ component of the claudin family, in terms of wound-closure dynamics (Fig. S1, A–D).

Altogether, these results show that SJ loss of function leads to dramatic defects in wound-closure dynamics. In particular, the wound-expansion phenotype observed in the strong mutants is remarkably different from the phenotype previously described in mutants for other wound-closure players such as AJs and actomyosin (Wood et al., 2002; Abreu-Blanco et al., 2012; Fernandez-Gonzalez and Zallen, 2013; Hunter et al., 2015; Matsubayashi et al., 2015).

SJ mutants show defective actomyosin dynamics

To determine why *kune* mutants do not efficiently close wounds, we first looked at the actomyosin cable that assembles at the wound edge. We quantified the intensity levels of our F-actin reporter at the wound edge in the first 30 min of wound closure, the time frame when the actin cable assembles. In the WT, F-actin levels gradually increased at the wound edge between 5 and 30 min post wounding (mpw), which is consistent with the formation of the actin cable and the beginning of wound contraction (Fig. 2 I). In contrast, in *kune*, F-actin levels were significantly decreased compared with the WT at 20 and 30 mpw (Fig. 2 I). These time points seem to coincide with the beginning of the expansion phenotype detected in *kune* strong mutants but slightly after the first defects in wound contraction (compare Fig. 2 F with Fig. 2 I). When measuring F-actin intensity in cells before wounding, we found no difference between controls and *kune* (Fig. 2 I), suggesting that Kune is required to form a functional actin cable but does not significantly influence F-actin dynamics in uninjured tissue.

Next, we investigated whether nonmuscle myosin-2 (hereafter called myosin), another component of the actomyosin cable required for its contractility and function (Abreu-Blanco et al., 2012; Fernandez-Gonzalez and Zallen, 2013), is also affected in *kune* mutants. We used the myosin heavy-chain endogenous reporter *zipper::GFP* (*zip::GFP*; Lye et al., 2014) and imaged wounded live embryos as described above. As seen for actin, myosin levels before wounding were similar between control and *kune* (Fig. 3 C). At 10 and 20 mpw, myosin accumulated at the wound edge in both controls and *kune* mutants, but at 30 mpw, the average myosin fluorescence intensity was significantly decreased in *kune* in comparison with controls (Fig. 3, A–C). As for F-actin, this decrease in myosin fluorescence in *kune* mutants seemed to occur approximately at the same time as when the wound started to expand, i.e., slightly later than when the wound contraction defects were evident (Fig. S2, A and B).

Actin-rich protrusions such as filopodia and lamellipodia are also required for proper wound-closure kinetics (Abreu-Blanco et al., 2012). Therefore, we investigated whether these protrusions were affected in *kune* mutants. We analyzed the area of protrusions in different time points after wounding, similar to what has been described previously (Abreu-Blanco et al., 2012; Zulueta-Coarasa et al., 2014), in both controls and *kune* mutants marked with our F-actin reporter (Fig. S2, C and D). We found no significant differences in protrusive activity between controls and *kune* mutants, suggesting that the *kune* wound-closure phenotype is not due to defects in these cellular structures. Altogether, we show that in the absence of functional SJs, cells at the wound edge develop impaired actomyosin dynamics shortly after the first wound-closure phenotypes appear.

Junctional dynamics at the wound edge are altered in *kune* mutants

Next, we followed the dynamics of SJ components at the wound edge. We analyzed the localization of the transmembrane SJ proteins Neurexin-IV (Nrx-IV) and Neuroglian (Nrg), whose mammalian homologues are present at paranodal junctions (Banerjee et al., 2006). We used protein trap transgenic lines expressing the functional Nrx-IV and Nrg proteins fused to GFP under the control of their endogenous promoters (Morin et al., 2001; Buszczak et al., 2007; Oshima and Fehon, 2011) and combined them with *Cherry::Moesin* to compare their localization with the actin cable. As expected from previous research (Nelson et al., 2010), already before wounding, Nrx-IV–GFP and Nrg-GFP intensities were significantly decreased in *kune* mutants when compared with WT (Fig. 4, B, E, and G; and Fig. S3 G). Furthermore, whereas in controls, these proteins concentrated at the apical region of the membrane, in *kune* mutants, they spread along the apical–basal axis (Fig. 4, A″, B″, C′, D″, E″, F′, and I; and Fig. S3, A′–F and I), also corroborating previous research (Nelson et al., 2010). Notably, at 10 and 30 mpw, both in WT and *kune*, Nrx-IV–GFP and Nrg-GFP levels decreased significantly at the wound edge (Fig. 4, A, A′, B, B′, C, D, D′, E, E′, and F; Fig. S3, A–F; and Videos 2 and 3). To quantify this, we compared Nrx-IV–GFP levels at the wound edge to the levels before wounding (Fig. 4 H). At 10 mpw, Nrx-IV–GFP intensity exhibited a 0.6-fold decrease relative to levels before wounding both in control and *kune* embryos. At 30 mpw, Nrx-IV–GFP intensity decreased even further in controls (reaching a fold change of 0.35), whereas in *kune*, this value was significantly higher than in controls (0.54-fold change), suggest-

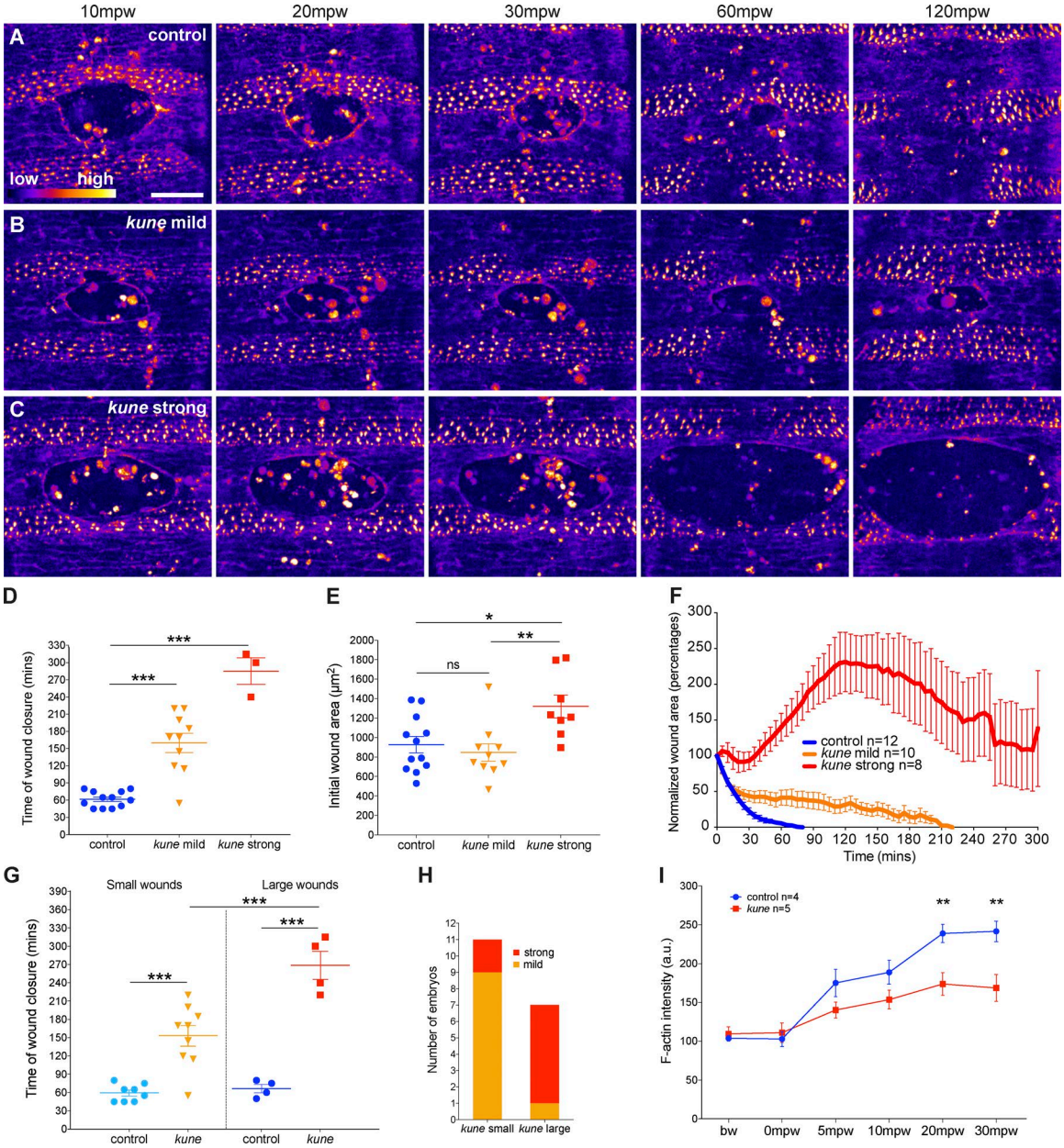

Figure 2. ***kune* mutants show altered wound-closure dynamics and actomyosin cable defects. (A–C)** Confocal images of the epidermis in control (A), *kune* mild mutant (B), and *kune* strong mutant embryos (C) expressing *Cherry::Moesin* labeling F-actin after laser wounding. Images are maximum Z projections of 49 slices (17-µm-thick stack) and pseudocolored in a color gradient (from lower intensities in blue to higher intensities in yellow). In all genotypes, F-actin accumulates at the wound edge at 10 mpw, and at 20 mpw, the wound starts contracting. At 120 mpw, the wound has closed in control embryo, whereas in the *kune* mild embryo, the wound has not closed, and in *kune* strong embryo, the wound size has increased. Bar, 20 µm. **(D)** Graph of average time of wound closure in control and *kune* mild and strong mutants. Note that from the total number of embryos analyzed, five *kune* strong wounds did not close and thus were not considered in this analysis. **(E)** Graph of average initial wound area in control and *kune* mild and strong mutants. **(F)** Graph of average wound area over time shows that *kune* mutants have altered wound-closure dynamics when compared with controls. In *kune* mild mutants, wounds closed slower than in controls. In *kune* strong mutants, wounds stopped contracting between 20 and 40 mpw, increased their area until ∼120–180 mpw, and then decreased their wound size again. **(G)** Graph of average time of wound closure in control and *kune* mutants divided in groups according to initial wound area (small wounds = 468–1,100 µm^2; large wounds = 1,101–1,820 µm^2). Note that from the total number of embryos analyzed, two *kune* small wounds and three *kune* large wounds did not close and were not considered in this analysis. **(H)** Graph showing the number of *kune* embryos showing a mild and strong phenotype according to initial wound area. **(I)** Graph of average F-actin intensity levels in the cortical region of cells before wounding (bw) and at the wound edge in control and *kune* embryos. F-actin intensity is significantly lower in *kune* than in controls at 20 and 30 mpw. Unpaired *t* test corrected for multiple comparisons using the Holm-Sidak method was performed to test for significant differences between groups in D, E, and G. *, P < 0.05; **, P <0.01; ***, P < 0.001. *n* = 12 embryos (control); *n* = 10 embryos (*kune* mild); *n* = 8 embryos (*kune* strong); *n* = 8 embryos (control small); *n* = 9 embryos (*kune* small); *n* = 4 embryos (control large); *n* = 4 embryos (*kune* large). A two-way ANOVA and a Sidak multiple comparison test were used to test for significant differences between groups in I. **, P < 0.01. *n* = 4 embryos (control); *n* = 5 embryos (*kune*). Error bars represent SEM.

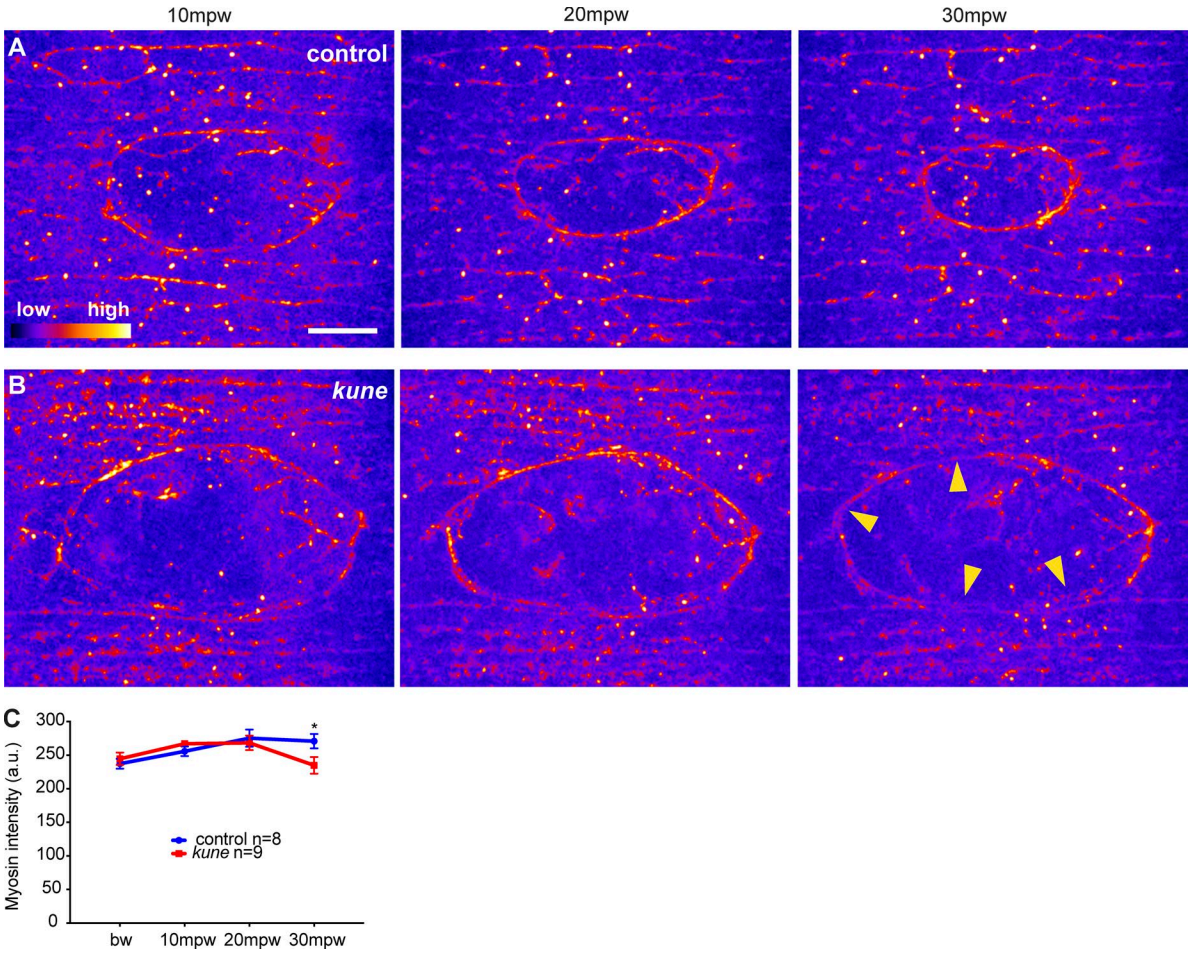

Figure 3. **Myosin localization is altered in *kune* mutant embryos. (A and B)** Confocal images of the epidermis in control (A) and *kune* mutant embryos (B) expressing *zip::GFP* labeling myosin before and after laser wounding. Images are maximum Z projections of 29 slices (10-µm-thick stack) and pseudocolored in a color gradient (from lower intensities in blue to higher intensities in yellow). Myosin accumulates at the wound edge shortly after injury. Whereas in controls, myosin is maintained during the first 30 mpw, in *kune* mutant embryos, myosin decreases at 30 mpw (yellow arrowheads in B). Bar, 10 µm. **(C)** Graph of average zip::GFP intensity levels in the cortical region of cells before wounding (bw) and at the wound edge in control and *kune* embryos. Myosin intensity is significantly lower in *kune* than in controls at 30 mpw. A two-way ANOVA and a Sidak multiple comparison test were used to test for significant differences between groups. *, $P < 0.05$. $n = 8$ embryos (control); $n = 9$ embryos (*kune*). Error bars represent SEM.

ing that Nrx-IV dynamics at the wound edge is affected by Kune loss of function. Furthermore, in *kune*, some cells at the wound edge accumulated Nrx-IV–GFP spots that colocalized with the actin cable, whereas in controls, this was not evident (Fig. 4, A′, A″, B′, B″, C, C″, D′, D″, E′, E″, F, and F′; and Videos 2 and 3). Similar results were obtained for Nrg-GFP (Fig. S3 H). These observations show that upon wounding, Nrx-IV–GFP and Nrg-GFP are down-regulated at the wound edge and that Kune loss of function affects the dynamics of these SJ proteins in this region.

To exclude the possibility that the ablation laser induces bleaching artifacts that lead to the observed down-regulation of these reporters at the wound edge, we stained wounded WT and *kune* embryos using an antibody that recognizes the SJ component Coracle and an F-actin marker. We found that similar to Nrx-IV–GFP and Nrg-GFP, Coracle was mostly excluded from the wound edge both in WT and *kune*, not colocalizing with the actin cable (Fig. S3, J and K).

We next investigated whether SJ loss of function affects cadherin-based AJs. AJs are also down-regulated at the wound edge, and their remodeling is required for proper actomyosin cable formation (Carvalho et al., 2014; Hunter et al., 2015; Matsubayashi et al., 2015). We imaged control and *kune* mutant embryos expressing the E-cadherin (E-cad) reporter *ubi–E-cad::GFP* (Oda and Tsukita, 1999). As previously reported, in controls, E-cad was down-regulated at the wound margin shortly upon laser wounding, only accumulating at the contact points between leading edge cells (Fig. 5, A, B, and E). In *kune*, E-cad intensity also decreased at the wound edge, but the fold change was significantly higher than in controls at 30 mpw (Fig. 5, C–E), suggesting that Kune loss of function interferes with E-cad remodeling at the wound edge. Interestingly, both the intensity levels and the apical localization of E-cad before wounding were unaltered in these mutants (Fig. 5 F), indicating that SJs do not affect AJ localization and polarity in the uninjured epithelium.

These results show that Kune loss of function leads to the mislocalization of both SJ and AJ components at the wound edge and that SJs are actively regulated at this region.

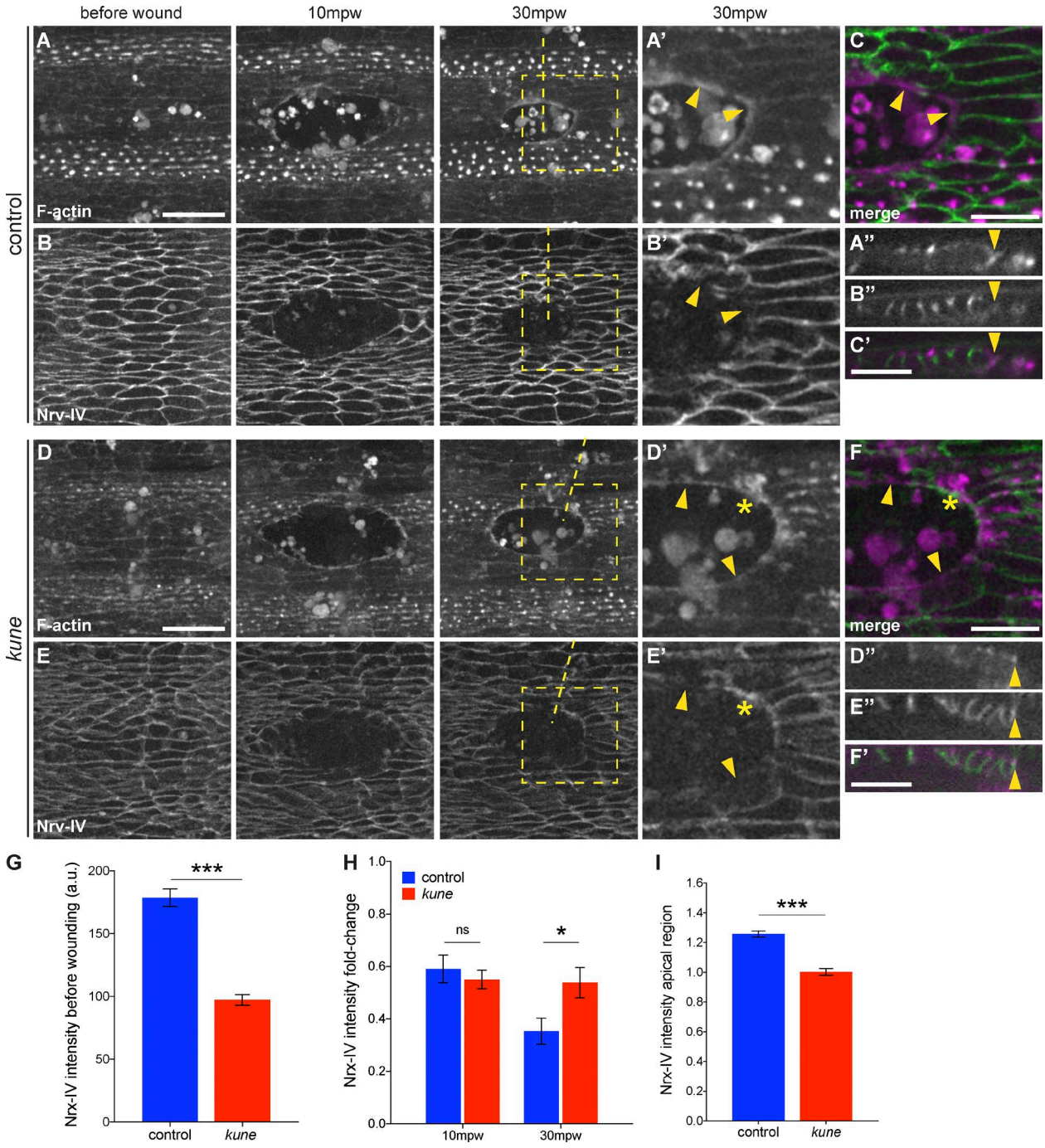

Figure 4. **The SJ component Nrx-IV is mislocalized at the wound edge in *kune* mutants. (A–F)** Confocal images of the epidermis during wound closure in control (A–C) and *kune* strong mutant embryos (D–F) expressing *Cherry::Moesin* labeling F-actin (A, A', A'', D, D', and D'') and *Nrx-IV–GFP* (B, B', B'', E, E', E'') before and upon laser wounding. **(C, C', F, F')** Merged images. **(A, A', B, B', D, D', E, and E')** Maximum Z projections of 61 slices (22-µm-thick stack). **(A'', B'', C', D'', E'', and F')** YZ sections marked by dashed lines shown in 30-mpw panels. Arrowheads in A'', B'', C', D'', E'', and F' mark the wound edge. Dashed squares mark zoomed regions shown in A', B', D', and E'. Bars: 20 µm (A, B, D, and E); 10 µm (A', A'', B', B'', C, and C'). Upon wounding, Nrx-IV decreases at the wound edge compared with cells away from the edge, mostly not colocalizing with the actin cable (arrowheads in A', B', C, D', E', and F). In *kune* mutants, Nrx-IV–rich accumulations are visible at the wound edge at 30 mpw, colocalizing with the actin cable (asterisks in D', E', and F). **(G)** Graph of average Nrx-IV–GFP intensity levels before wounding in control (40 junctions from four embryos) and *kune* mutants (50 junctions from five embryos). **(H)** Graph of fold change decrease in Nrx-IV–GFP intensity in wound edge junctions at 10 and 30 mpw (compared with before wounding), in control (15 junctions from four embryos), and *kune* embryos (14 junctions from three embryos). **(I)** Graph showing Nrx-IV intensity at the apical side of cells before wounding in control (30 junctions from six embryos) and *kune* embryos (30 junctions from six embryos). An unpaired *t* test (G and I) and a two-way ANOVA and multiple comparisons Sidak test (H) were performed to test for significant differences between groups. *, P < 0.05; ***, P < 0.0001. Error bars represent SEM.

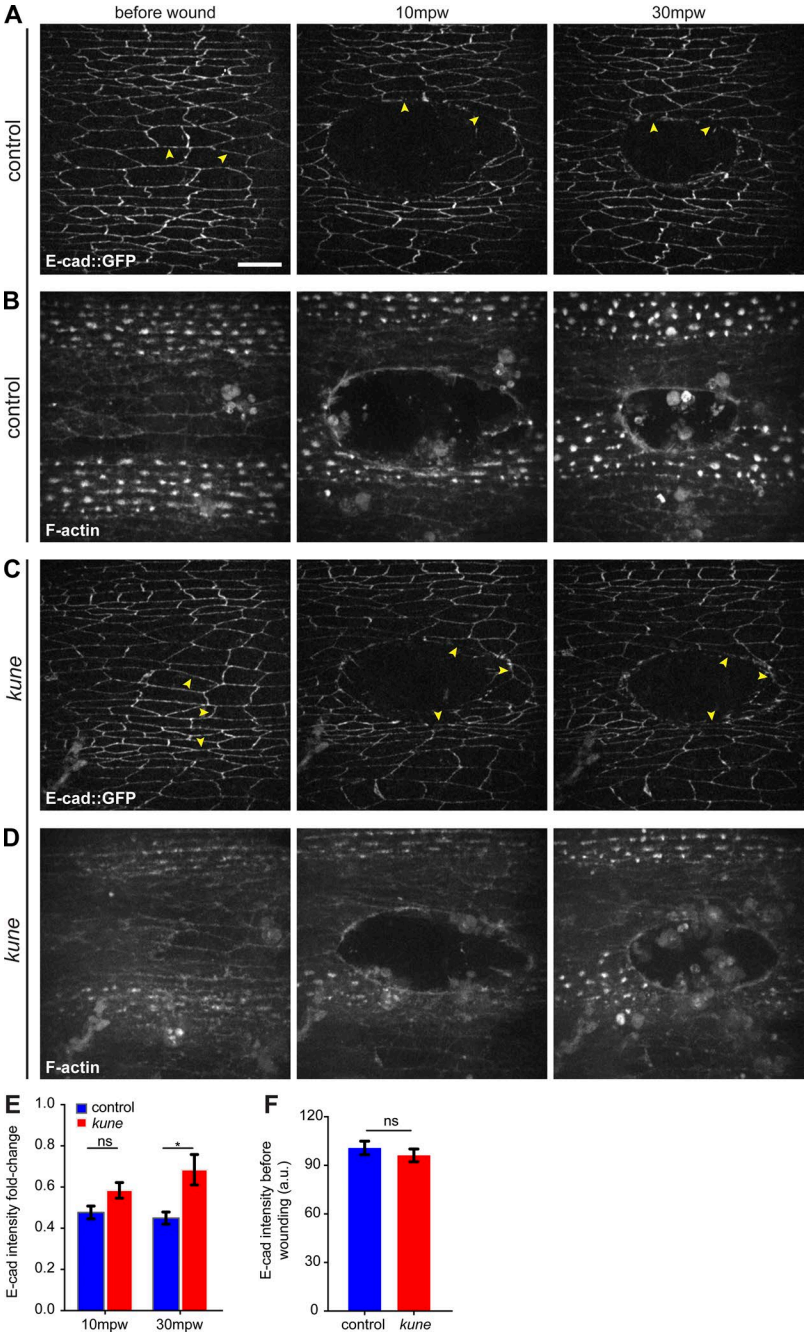

Figure 5. **E-cad localization in control and *kune* mutants. (A–D)** Confocal images of the epidermis during wound closure in control (A and B) and *kune* strong mutants (C and D) expressing *ubi–E-cad::GFP* (A and C) and *Cherry::Moesin* labeling F-actin (B and D) before and upon laser wounding. Images are maximum Z projections of 40 slices (14-µm-thick stack). Upon wounding, E-cad intensity decreases at cell boundaries facing the wound edge in controls and *kune* mutants (arrowheads mark the same junctions before and after wounding in each embryo). Bar, 10 µm. **(E)** Graph of fold change decrease in E-cad::GFP fluorescence intensity in cell boundaries at the wound edge at 10 and 30 mpw (compared with before wounding), in control (35–39 junctions from six embryos), and *kune* embryos (36–42 junctions from seven embryos). **(F)** Graph of average E-cad::GFP fluorescence intensity in cells before wounding in control (56 junctions from six embryos) and *kune* embryos (59 junctions from seven embryos). A two-way ANOVA with a Sidak multiple comparisons test (E) and an unpaired *t* test (F) were performed to test for significant differences between groups. *, $P < 0.05$. Error bars represent SEM.

SJs are required both in wound edge cells and in cells not at the wound edge for efficient wound closure

We can imagine two scenarios to explain the influence of SJs on wound closure. One is that SJ loss of function impairs the adhesion between cells, thereby influencing the cohesion and mechanics of the epidermal tissue as a whole and hence its response to injury; in this scenario, the defects in actomyosin and junction dynamics would be a consequence of impaired tissue mechanics. Alternatively, SJs might influence actomyosin cable function by directly regulating actin and/or myosin. To address these hypotheses, we investigated whether the effect of *kune* loss of function on the actomyosin cable is autonomous to each cell or, in contrast, nonautonomous. We knocked down Kune in a specific subset of epidermal cells using RNAi by expressing double-stranded RNA (dsRNA) against *kune* through the Gal4/UAS system (St Johnston, 2013). We expressed Kune UAS-dsRNA under the control of the *engrailed-Gal4* (*en-Gal4*) promotor, which induces expression in a segmented pattern in the embryonic epidermis (Brand and Perrimon, 1993). This allowed us to image the behavior of both WT and *kune*-deficient cells in the same embryo and observe how that affects wound closure and actin cable formation. To validate this technique, we fixed unwounded control and Kune-RNAi embryos and stained them for the SJ protein Coracle. As expected, Coracle localization was down-regulated in the cells expressing *kune* RNAi but not in surrounding WT cells (Fig. S4, A and B), showing that *kune* loss of function impairs SJ localization in a cell-autonomous manner.

Next, we followed wound closure in *kune* RNAi embryos. All epidermal cells expressed *GFP::Moesin*, an F-actin reporter (Kiehart et al., 2000), and the segmented patches of *kune* RNAi (or control RNAi) cells additionally expressed *Cherry::CAAX*, a membrane marker (Sens et al., 2010), to distinguish RNAi-expressing from RNAi-nonexpressing cells. We examined wound closure in wounds inflicted in two different regions of the epidermis: wounds located between two *en-Gal4* stripes, in which wound edge cells did not express *kune* RNAi (Kune RNAi minus; Fig. 6, A and C; and Video 4); and wounds spanning an *en-Gal4* stripe, in which some of the wound edge cells expressed *kune* RNAi (Kune RNAi plus; Fig. 6, B and D; and Video 5). Strikingly, both types of wounds led to closure defects similar to *kune* mutants. Kune RNAi plus wounds showed the strongest phenotype, resembling *kune* strong mutants, whereas Kune RNAi minus wounds developed a phenotype similar to *kune* mild mutants (compare Fig. 6 [A–F] with Figs. 2 [B–F] and S4 [C and D]). As in *kune* mutants, the wound size also influenced closure time in Kune RNAi embryos (Fig. 6, E and F; and Fig. S4, C and D). First, we have to consider that all minus wounds had an area <1,100 µm^2 due to the small space between two *en-Gal4* stripes. We found that the wound-closure time of Kune RNAi–plus large wounds (>1,100 µm^2) was significantly higher than the wound-closure time of Kune RNAi–plus and –minus small wounds (<1,100 µm^2). However, the closure time of Kune RNAi–minus and –plus small wounds was similar (Fig. S4 D). These results support the hypothesis that SJs are necessary for wound healing not only in wound-edge cells but also in the surrounding tissue.

To determine whether Kune loss of function affects the actin cable cell autonomously, we measured F-actin intensity in the plus wounds and compared *en-Gal4*–positive (Kune RNAi) with *en-Gal4*–negative (WT) regions of the cable. Interestingly, F-actin levels were not different between Kune RNAi and WT cells in the same wound (Fig. 6 G), suggesting that the effects of Kune loss of function on the actin cable are not cell autonomous. Altogether, these data indicate that SJs are not required for actomyosin cable function in a cell-autonomous manner, suggesting SJs do not directly target the cytoskeleton. This favors the hypothesis that the impact of SJs on cable contraction is a consequence of defects at the tissue level.

SJs regulate cellular shapes and rearrangements

Cell shape changes and rearrangements have been shown to promote efficient wound closure (Razzell et al., 2014). To address whether SJs regulate cell shape, we imaged unwounded *ubi-E-cad::GFP* transgenic embryos, which allow us to detect cell boundaries, and compared cell apical area and elongation (i.e., aspect ratio) in control with *kune* mutant embryos (Fig. 7, A and B). At this embryonic stage, the epidermis is composed of two types of cells that give rise to denticle-containing and denticle-free (or smooth) cells in the larva and thus exhibit distinct cell shapes (Price et al., 2006; Walters et al., 2006). We found that the average area of smooth cells in *kune* mutants was significantly larger than in controls (Fig. 7 C), while the average aspect ratio was significantly increased in denticle cells (Fig. 7 D). This means that *kune* denticle cells are more stretched along the dorsal–ventral axis than WT cells while keeping their average area; conversely, *kune* smooth cells maintain their aspect ratio but increase their size when compared with WT cells.

To determine whether this effect was cell autonomous, we performed the same measurements in embryos expressing *kune* RNAi in *en-Gal4* stripes (Fig. 7, E and F) and also found cell shape phenotypes. Smooth cells showed larger areas in *kune* RNAi than in control embryos, whereas both smooth and denticle cells showed increased aspect ratios when compared with control embryos (Fig. 7, G and H). Interestingly, when we analyzed each cell row in separate to distinguish *kune* RNAi–positive from *kune* RNAi–negative cells, we observed that even the latter showed significant differences in cell area and aspect ratio when compared with controls (Fig. S5, C–F). Furthermore, the specific cell rows showing altered cell shapes varied between *kune* RNAi and *kune* mutants (Fig. S5, A and B). These results suggest that SJs influence epithelial cell shapes in a cell-nonautonomous manner, likely by regulating the properties of the epithelium at the tissue level.

We then checked whether cellular rearrangements are altered in *kune* mutants during wound closure. We measured the number of neighbor cells of each cell adjacent to the wound margin during the first 45 mpw, when wound-closure defects appear in the *kune* mutants. We found that cells keep the average number of neighbors approximately constant during this time period (five to six neighbors per cell; Fig. 7 K). Also, the number of cells in the first two rows closer to the wound margin does not change significantly (Fig. 7 L), suggesting that cellular rearrangements do not occur at a large scale. However, controls exhibited significantly more neighbor exchange events than *kune* mutants in cells at the wound edge (Fig. 7, I, J, and M). Moreover, the fraction of cells undergoing cell neighbor exchange events is higher in controls than in *kune* mutants (Fig. 7 N). In conclusion, these data suggest that SJs are required for proper cellular rearrangements during wound closure.

SJs influence the mechanical properties of the embryonic epidermis

It is now accepted that cell and tissue shapes highly rely on their mechanical properties (Paluch and Heisenberg, 2009). The generation and transmission of forces in an epithelial cell are mainly controlled by the actomyosin cytoskeleton and the AJs, while the contribution of OJs is still not clear (Sluysmans et al., 2017). Considering that Kune seems to regulate cell shapes and wound closure at the tissue level, we hypothesized that SJs might regulate the mechanical properties of the epithelium. To estimate tissue physical properties, we used the laser ablation technique and modeled the tissue as a viscoelastic material as described previously (Paluch and Heisenberg, 2009; Campàs, 2016). Immediately (in the first 30 s) after a small laser cut, the tissue, which is under homeostatic tension, relaxes and opens up to a maximum point before an active repair response begins. This fast response allows us to estimate not only the homeostatic tension of the tissue but also its effective viscoelastic properties at small time scales. Using control and *kune* mutant embryos, we performed laser cuts at the junction between two cells as described previously (Behrndt et al., 2012) and measured the displacement along time of the two vertices associated with the

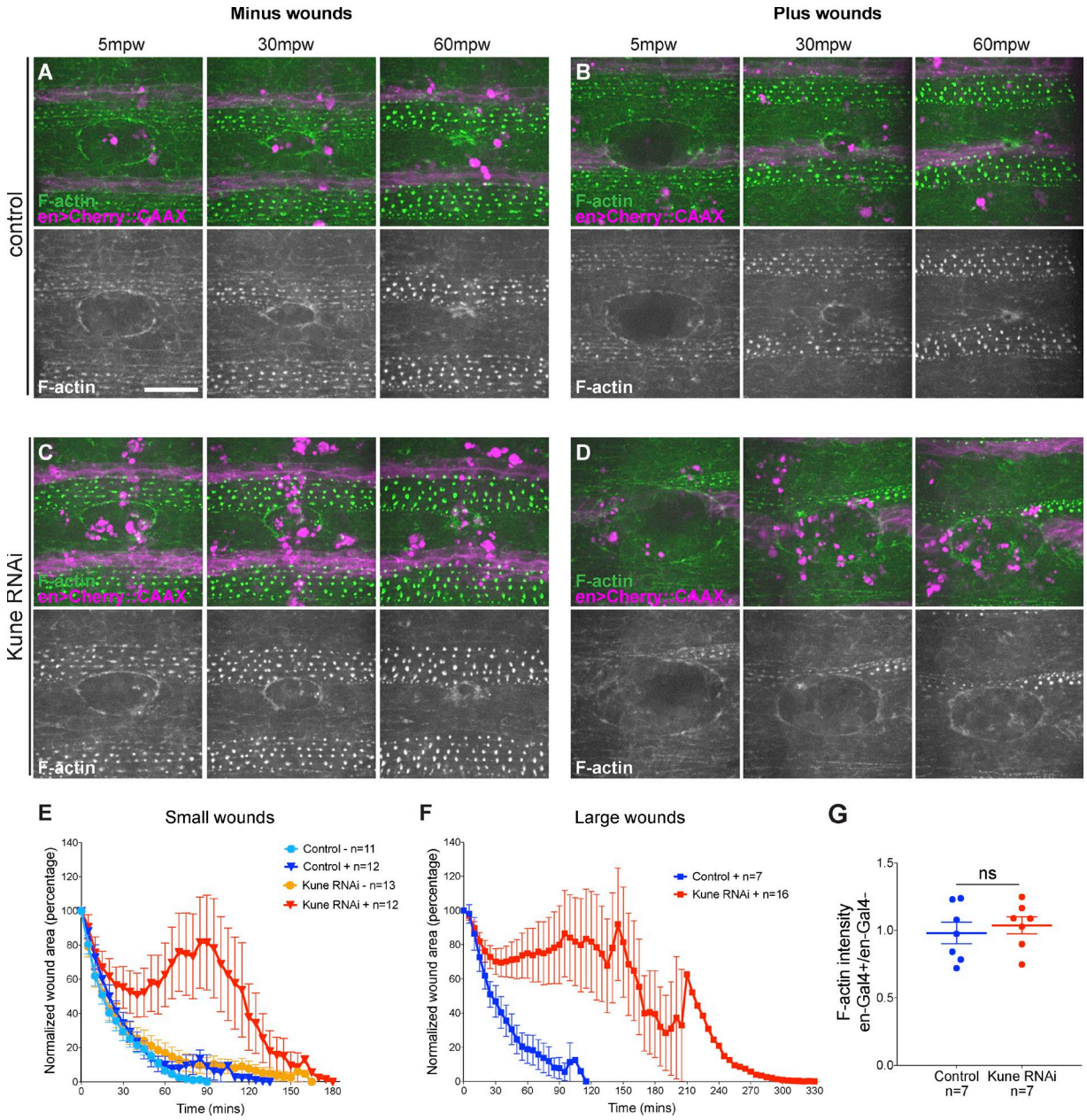

Figure 6. **Kune is required for wound closure in cells not directly at the wound edge. (A–D)** Confocal images of the epidermis during wound closure in control (A and B) and *kune* RNAi embryos (C and D) expressing *GFP::Moesin* labeling F-actin and *Cherry::CAAX* under control of the *en-Gal4* promotor labeling cell membranes upon laser wounding. Top: Merged images (green, F-actin; magenta, *en-Gal4*). Bottom: F-actin. Images are maximum Z projections of 50 slices (17.6-µm-thick stack). **(A and C)** Embryos with wounds located between two *en-Gal4*–expressing stripes (minus). **(B and D)** Embryos with wound spanning one *en-Gal4*–expressing stripe (plus). Bar, 20 µm. **(E and F)** Graphs of average wound area over time in small (initial wound area <1,100 µm^2) and large wounds (initial wound area >1,100 µm^2) in *en-Gal4*–minus and –plus embryos. *kune* RNAi–plus embryos show a stronger phenotype than *kune* RNAi–minus embryos. **(G)** Graph of F-actin ratio at the wound edge in *en-Gal4*–positive versus *en-Gal4*–negative regions in control and *kune* RNAi–plus embryos at 30 mpw. An unpaired *t* test was used to test for significant differences between groups. ns, P > 0.05. *n* = 7 embryos (control); *n* = 7 embryos (*kune* RNAi). Error bars represent SEM.

epidermal cells subjected to laser cutting (Fig. 8, A and B; and Video 6). We observed that *kune* mutant cells seemed to relax faster than control cells, whereas the maximum displacement was approximately the same (Fig. 8 C). The simplest possible viscoelastic model that describes this relation is the Kelvin-Voigt (KV) model (see Materials and methods; Fernandez-Gonzalez et al., 2009; Mayer et al., 2010). Using this model, the displacement of the vertices is given by the equation $d = d_M(1 - e^{-t/\tau})$, where d_M is the maximum displacement, and τ is the retardation time. A fit of our data gives us $\tau = 13.9 \pm 2.2$ s and $d_M = 2.74 \pm 0.15$ µm for controls versus $\tau = 9.0 \pm 1.2$ s and $d_M = 2.77 \pm 0.09$ µm for *kune* (Fig. 8 C). The KV model tells us that

$$\tau = \frac{\eta}{G}$$

and

$$d_M = \frac{F_0}{G},$$

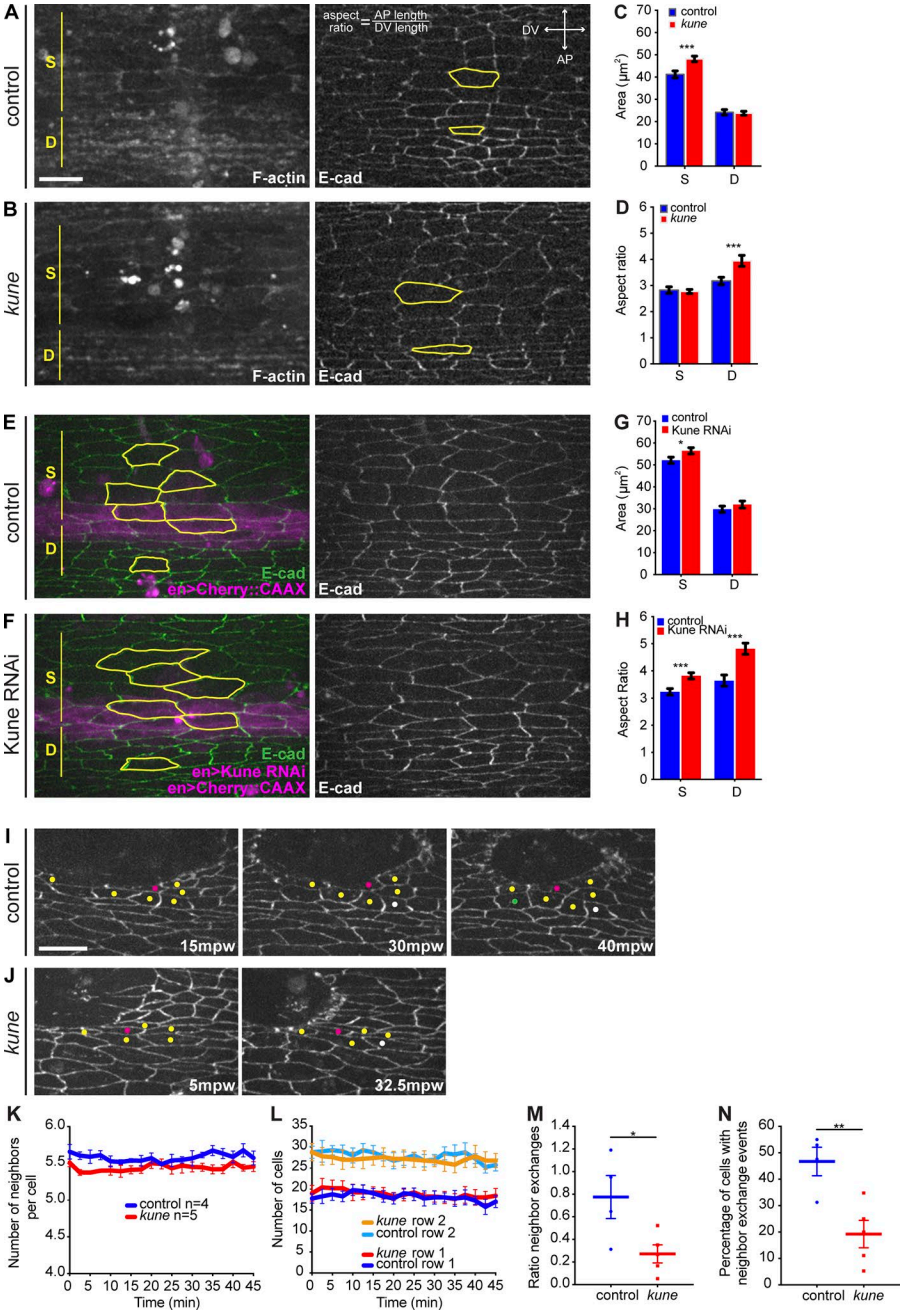

Figure 7. **Kune loss of function modifies cellular shapes. (A and B)** Confocal images of the epidermis in control (A) and *kune* embryos (B) expressing *Cherry::Moesin* labeling F-actin (left) and *ubi-E-cad::GFP* labeling E-cad (right). **(C and D)** Average area (C) and average aspect ratio (D) of smooth and denticle cells in control (48 smooth cells and 24 denticle cells from three embryos) and *kune* embryos (64 smooth cells and 32 denticle cells from four embryos). **(E and F)** Confocal images of the epidermis in control (E) and *kune* RNAi embryos (F) expressing *ubi-E-cad::GFP* labeling E-cad and *Cherry::CAAX* under control of the *en-Gal4* promotor labeling cell membranes. Left: Merged images. Right: E-cad. **(G and H)** Average area (G) and average aspect ratio (H) of smooth and denticle cells in control (48 smooth cells and 24 denticle cells from three embryos) and *kune* RNAi embryos (96 smooth cells and 48 denticle cells from six embryos). **(I and J)** Confocal images of the epidermis in control (I) and *kune* embryos (J) expressing *E-cad::GFP* at different time points of wound closure depicting neighbor exchange events. Magenta dots mark the cell analyzed, yellow dots mark neighbors, white dots mark cells that lose contact with the cell analyzed, and the green dot marks a cell establishing a new connection. Bars, 10 µm. **(K and L)** Number of neighbors in cells at the row adjacent to the wound edge (K) and number of cells in the first two rows closer to the wound edge (L) in control ($n = 4$) and *kune* ($n = 5$) embryos. **(M and N)** Ratio of neighbor exchange events (M) and percentage of cells undergoing neighbor exchange events (N) in control ($n = 4$) and *kune* ($n = 5$) embryos. An unpaired *t* test was performed to test for significant differences between groups. *, $P < 0.05$; **, $P < 0.01$; ***, $P < 0.001$. Error bars represent SEM. Images are maximum Z projections of 49 slices (17-µm-thick stack). Representative cells are outlined. S, smooth cells; D, denticle cells; DV, dorsal–ventral axis; AP, anterior–posterior axis.

where η is the viscous drag coefficient, G is the stiffness, and F_0 is the homeostatic tension. Our results suggest that even if the tension F_0 and the stiffness G are altered in the mutant, their ratio remains approximately constant. However, the smaller retardation time in the mutant can be explained either by a larger stiffness (and consequently larger tension) or by a decrease in the viscous drag coefficient.

A careful inspection of the average displacement for the initial time window ($t < 20$ s) is also compatible with a weak power law model (Fig. 8 D; Ma et al., 2009), which can be characterized by the equation

$$d = \frac{F_0}{G'}\left(\frac{t}{\tau'}\right)^{\alpha},$$

where G' and τ' are scale factors for stiffness and time (see Materials and methods). When α approaches 0, the system behaves more like an elastic solid, whereas when α tends to 1, the system behaves more like a viscous fluid. Interestingly, the power law exponents for controls and *kune* are approximately the same ($\alpha \approx 0.44$), revealing systems with both solid and fluidic behaviors. These values are similar to the ones obtained previously for the amnioserosa cell junctions in the *Drosophila* embryo (Ma et al., 2009). However, the observation that the prefactor of this equation, given by $F_0/(G'^{1-\alpha}\eta'^{\alpha})$, is higher in the mutant than in controls (Fig. 8 D) may be justified by a lower effective viscous drag coefficient or a higher tension in the mutant as seen with the KV model.

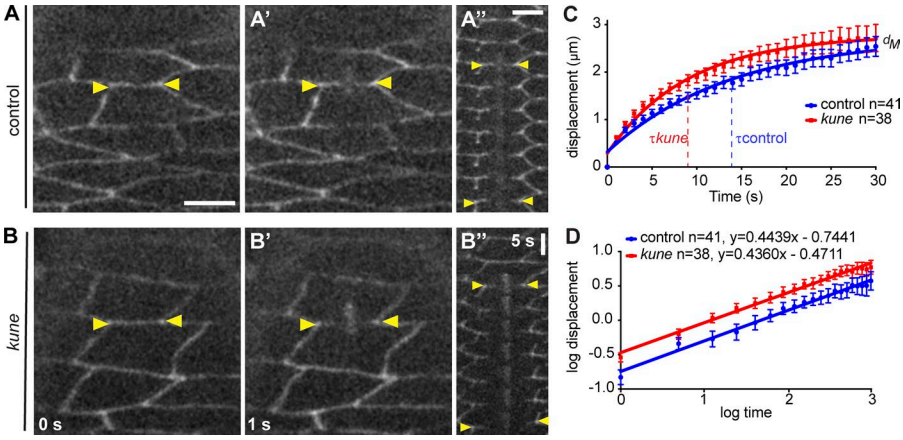

Figure 8. **Mutants for the claudin Kune show altered mechanical responses to laser ablation. (A and B)** Confocal slices of control (A) and *kune* (B) ventral epidermis expressing *ubi-E-cad::GFP* before (A and B) and 1 s after a laser cut (A′ and B′). **(A″ and B″)** Corresponding kymographs showing vertex displacement over time (every 5 s). Arrowheads mark the vertices attached to the cut edge. Bars: 5 µm (A, A′, B, and B′); 2 µm (A″ and B″). **(C)** Graph shows the displacement of cell vertices over time upon laser cutting in control (n = 41 cells, blue line, circles) and *kune* (n = 38 cells, red line, squares). Note that in *kune* cells, vertices retract faster than in controls as evidenced by their different retardation times τ (controls = 13.9 s; *kune* = 9.0 s; P = 0.0466). Maximum displacements d_M (control = 2.74 µm; *kune* = 2.77 µm; P = 0.8508) were similar between both genotypes. **(D)** Graph of displacement over time after a logarithmic transformation of the values presented in graph (C) for the initial time window (t < 20 s) shows a power law behavior. The slopes of the regression lines obtained for controls and *kune* are approximately the same (0.44; P = 0.8338), whereas the intercept value is significantly different (control = −0.74; *kune* = −0.47; P < 0.0014). Error bars represent SEM. Extra sum of squares F test was applied to test for significant differences between genotypes.

These results suggest that SJs significantly impact the mechanical properties of the tissue either by increasing its homeostatic tension or by reducing its effective viscosity. Although we cannot exclude any hypothesis, we strongly favor the latter as it seems more compatible with the idea of defective junctions that are less able to sustain the membrane relaxation occurring after a laser cut and with the observation that mutant cells exhibit larger apical surface areas than WT cells.

Discussion

This study uncovers a novel role for SJs in regulating epithelial mechanics and efficient wound closure in the *Drosophila* embryonic epidermis. In simple epithelia, the main driving force to resolve a small lesion in a scar-free manner is proposed to be actomyosin contractility at the wound edge (Garcia-Fernandez et al., 2009; Zulueta-Coarasa and Fernandez-Gonzalez, 2017). Cellular rearrangements and shape changes have also been found to contribute for wound closure (Razzell et al., 2014). According to our data, SJs seem to be more important for these latter processes. Although the absence of functional SJs affects the actomyosin cable and junctional dynamics at the wound edge, these defects are milder than the ones we would expect considering the severity of the wound closure phenotype. In addition, the observed decrease in F-actin at the cable appears to be noncell autonomous, suggesting that it might be a consequence of defects at the tissue level. Finally, the wound-closure dynamics in SJ mutants is very different from the loss-of-function phenotypes of actomyosin or AJs (Wood et al., 2002; Abreu-Blanco et al., 2012; Fernandez-Gonzalez and Zallen, 2013; Hunter et al., 2015; Matsubayashi et al., 2015). Instead of the typical slower contraction described in actomyosin and *E-cad* mutants, in the strong SJ mutants, wounds undergo a stage of great expansion. Further supporting our hypothesis, impairing the function of the claudin Kune in only a subset of epidermal cells leads to wound-closure defects similar to the ones seen in *kune* mutants. Notably, a phenotype was detected even when Kune-deficient cells were part of the tissue surrounding the wound but not directly at the leading edge that forms the actomyosin cable. Recently, the classical idea that the actomyosin cable is the driving force for wound closure has been challenged. Ducuing and Vincent (2016) have proposed that this structure rather acts as a passive force field that protects cells from the forces present at the tissue scale instead of working like an active purse string. Our data are compatible with this view. Actomyosin cable contraction might not be as crucial as previously anticipated, and tissue level rearrangements and adhesive forces regulated by SJs and AJs might be key drivers of wound closure in simple epithelia.

Still, we cannot exclude that SJ dynamics at the wound edge are needed to form a proper actomyosin cable as shown for AJs (Carvalho et al., 2014; Hunter et al., 2015; Matsubayashi et al., 2015). Dlg, an SJ scaffolding protein, has been proposed to counteract myosin activity in the *Drosophila* embryonic epidermis (Simone and DiNardo, 2010). Similarly, the observed accumulation of Nrx-IV and Nrg at the wound edge in *kune* mutants could interfere with myosin activity at the cable. It has also been shown that cellular rearrangements during wound closure depend on myosin function (Razzell et al., 2014). Therefore, it is also possible that SJs control cellular rearrangements by directly regulating myosin activity. Thus, a direct molecular link between SJs and the actomyosin cytoskeleton should be tested in future studies.

Recent research in mammalian systems has already proposed a link between OJs and wound healing, but functional research has only been attempted in in vitro systems (Volksdorf et al., 2017). In this study, we show for the first time that OJs are required for wound healing of simple epithelia in vivo.

Our study is also the first evidence that SJs play an important role in epithelial mechanics in *Drosophila*. In fact, our data suggest that the wound-closure phenotypes observed in SJ mutants are a consequence of defects in tissue mechanics already present in the unwounded tissue. When Kune is missing, epithelial cells develop altered geometries and reduce neighbor exchange events

during wound closure when compared with controls. Moreover, *kune* mutant cells react differently than WT cells to mechanical perturbation, leading us to propose that SJs contribute to the viscous drag component of the tissue. At the molecular and cellular level, the effective global viscosity at the cell membrane should be related to the physical properties of all junctions, e.g., their flexibility and ability of junctional molecules to bind or dissociate from each other. When SJs are defective, the physical connections between cells likely become weaker or looser, so a decrease in the global viscosity and in the stiffness of their membranes should be expected. However, our modeling is also consistent with *kune* mutants presenting higher tension and stiffness. Yet the observation that *kune* mutant cells exhibit larger apical surface areas, typically associated with lower tensions (Fanning et al., 2012; Choi et al., 2016; Tsoumpekos et al., 2018), strongly argues against this idea. Interestingly, recent studies have shown that the lack of zonula occludens (ZO) proteins at vertebrate TJs can either lead to increased tension in the *Xenopus laevis* embryo and in MDCK epithelial cells or to decreased tension in human endothelial cells (Tornavaca et al., 2015; Choi et al., 2016; Hatte et al., 2018). Therefore, this regulation might be context specific.

The influence of SJs on tissue mechanics is different from what has been shown for AJs: in AJ loss of function, cortical tension dramatically decreases, whereas viscoelastic properties are typically maintained (Paluch and Heisenberg, 2009). This might be, at least partially, because AJs and SJs connect differently to the cytoskeleton. Whereas AJs associate with actin, the links between OJs and the cytoskeleton are still poorly understood. In vertebrates, ZO scaffolding proteins also bind to actin, but their role in mechanotransduction is only beginning to be explored (Tornavaca et al., 2015; Choi et al., 2016; Sluysmans et al., 2017; Hatte et al., 2018). In *Drosophila*, the SJ components Nrg and Na^+/K^+ ATPase can associate with the spectrin-based cytoskeleton, which in turn plays mechanosensory functions and binds actin and myosin (Dubreuil, 2006; Meng and Sachs, 2012; Krieg et al., 2014). Therefore, it is possible that SJs are also able to transmit and/or sense mechanical cues but through different mechanisms than AJs. Finally, we should also note that the viscoelastic properties of cells and tissues in vivo have been mostly inferred indirectly, so the impact of both AJs and OJs for the viscoelastic behavior of tissues in the context of an organism is far from being characterized. Future studies combining quantitative and direct measurement methods with theoretical modeling should help us uncover these mysteries.

Materials and methods

Drosophila strains and genetics

Crosses were performed at 25°C or 29°C on standard *Drosophila* medium. The w^{1118} strain was used as control. All strains used were purchased from the Bloomington Drosophila Stock Center unless stated otherwise. Mutant alleles and chromosomal deletions used were $kune^{C309}$, $sinu^{nwu7}$, $sinu^{06524}$, pck^{G0012}, $Nrx\text{-}IV^{4304}$, $Nrx\text{-}IV^{EP604}$, $Nrx\text{-}IV^{EY06647}$, nrg^{14}, $nrv2^{k13115}$, $cora^{5}$, $vari^{f0033}$, gli^{1}, $dlg1^{EY05003}$, $dlg1^{2}$, $dlg1^{5}$, $crok^{KG06053}$, $cold^{f05607}$, *Df(2L)BSC255*, *Df(2R)BSC630*, *Df(2R)BSC630*, and *Df(2R)BSC26*. All alleles and deletions were crossed to balancer stocks that express GFP under the control of the *twist* promoter (Halfon et al., 2002), and homozygous mutant embryos were identified by the absence of GFP fluorescence. For the wounding assay, transallelic combinations or combinations with chromosomal deletions were used whenever possible to avoid effects of secondary mutations. For confocal imaging, mutant alleles were recombined with live reporter lines.

The live reporters used were *UAS-Cherry::Moesin* under the control of the *e22c-Gal4* promoter (Millard and Martin, 2008) or *sqh-GFP::Moesin* (Kiehart et al., 2000) to mark F-actin; $zip^{CPTI\text{-}100036}$*-GFP* (Lye et al., 2014) to mark myosin-2 heavy chain; *UAS-mCherry::CAAX* (Sens et al., 2010) or *UAS-GFP* to identify RNAi-expressing cells; *ubi-E-cad::GFP* (Oda and Tsukita, 1999) and *E-cad::GFP* (Huang et al., 2009) to mark E-cad; and *Nrx-IV-GFP* (CA06597) and *Nrg-GFP* (G305; Morin et al., 2001; Buszczak et al., 2007) to mark Nrx-IV and Nrg-GFP, respectively.

To knock down *kune* expression by RNAi, *UAS-kune-dsRNA-HMS01755* (TRiP; Harvard Medical School) was expressed under the control of the *en-Gal4* promoter to obtain a segmented knockdown in the epidermis. Controls were obtained by crossing *en-Gal4* flies with the RNAi control line containing the same insertion sites as the RNAi line (TRiP; Harvard Medical School).

Wounding assay

The wounding assay was performed as previously described (Campos et al., 2010; Geiger et al., 2011; Carvalho et al., 2014). Briefly, stage 15–16 embryos were collected from laying pots kept at 25°C overnight, dechorionated in 50% bleach, and rinsed extensively with water. Mutant embryos were aligned on a slide with a double-sided tape affixed to it and covered with halocarbon oil 700 (Sigma-Aldrich) and a coverslip. The embryos were wounded at 25°C by using a nitrogen laser-pumped dye laser (435 nm; Micropoint Photonic Instruments) connected to a Nikon/Andor Revolution XD spinning-disk confocal microscope with an electron-multiplying charge-coupled device (EMCCD) camera (iXon 897) using iQ software (Andor Technology) and using a 60× Plan Apochromat VC Perfect Focus System (PFS) 1.4 NA oil-immersion objective. After wounding, the coverslip was carefully removed, and the embryos were left to recover in a humid chamber at 20°C. The wounded embryos were scored under a stereo microscope for closed/open wounds 16 h later. Percent wound closure was calculated as the ratio of nearly hatching embryos with unclosed wounds over the total number of wounded embryos (dead animals were excluded). Fisher's exact test was performed to test for statistical significance.

Immunohistochemistry and imaging of fixed samples

Embryos at stage 15 were laser wounded and placed in a humid chamber to recover. Wounded embryos were transferred to a glass vial containing a mix of 1:1 heptane and 8% formaldehyde in PBS and fixed for 40 min, manually devitellinized, washed in PBST (PBS + 0.1% Triton X-100), incubated for 1 h in blocking solution (0.3% BSA + 0.3% Triton X-100 in PBS), which was followed by primary antibody and probe incubation overnight at 4°C. The primary antibodies and probes used were mouse anti-Coracle C-terminal (1:500; Developmental Studies Hybridoma Bank), rabbit anti-GFP (1:2,000; Invitrogen), and Alexa Fluor 594–conjugated

phalloidin (1:200; Invitrogen). Following incubation, embryos were washed in PBST, incubated in secondary antibodies conjugated to Alexa Fluor 488 or Alexa Fluor 568 (Invitrogen) for 2 h in blocking solution, washed in PBST, and mounted in 80% glycerol and 2% DABCO (Sigma-Aldrich). Imaging was performed on an LSM 710 confocal microscope (Zeiss) with a 63× Plan Apochromat 1.4 NA oil-immersion objective (Zeiss). Images were acquired using Zen software (Zeiss) and a step size of 0.37 µm.

Live imaging

Live imaging was performed as described previously (Geiger et al., 2011; Carvalho et al., 2014). Dechorionated stage 15 embryos were mounted on their ventral side on glass-bottomed culture dishes (MatTek) with embryo glue (double-sided tape diluted in heptane) and covered with halocarbon oil 27 (Sigma-Aldrich). Embryos were wounded as described above for the wounding assay except that the laser power was lower in order to inflict smaller wounds that are able to close during the imaging procedure. Time-lapse microscopy of transgenic embryos was performed at 25°C on a Nikon/Andor Revolution XD spinning-disk confocal microscope with an EMCCD camera (iXon 897) using iQ software and using a 60× Plan Apochromat VC PFS 1.4 NA oil-immersion objective, a 60× Plan Apochromat VC PFS 1.2 NA water-immersion objective, or a 100× Plan Apochromat PFS 1.4 NA oil-immersion objective (Nikon). Individual z slices with a step size of 0.36 µm (60× objectives) or 0.25 µm (100× objectives) were acquired every 1, 2.5, or 5 min for 60–300 min.

Laser-cutting experiments

Laser-cutting experiments were performed using a UV laser cutter setup as previously described (Behrndt et al., 2012) on both WT and *kune* mutant embryos expressing *ubi-E-cad::GFP* and *Cherry::Moesin* at stage 15 of embryonic development. Laser cuts were performed in ventral epidermal smooth cells at the level of the AJs by applying 50 UV pulses to two equidistant sites in a 2-µm-long line perpendicular to the junction. A single cell was cut per embryo. Images were acquired every 1 s for at least 1 min in an Andor Revolution spinning-disk confocal microscope with a Zeiss 100× 1.3 NA oil-immersion lens.

Image analysis and quantifications

All images were processed and analyzed using Fiji (ImageJ; National Institutes of Health [NIH]; Schindelin et al., 2012) except when mentioned otherwise.

Fluorescence intensity measurements

To measure F-actin and myosin intensities at the wound edge, maximum Z projections of *Cherry::Moesin*, *GFP::Moesin*, and *Zip::GFP* stacks were used after background subtraction. The wound edge and the cortical region of epithelial cells before wounding were outlined using a 5-pixel-wide segmented line, and the average intensity was obtained using the Measure tool. To obtain intensity values before wounding, 10 cells per embryo were measured. For F-actin quantifications, cells containing actin-rich denticle precursor structures were not included in the measurements as they mask the actin present at the cable and cell cortex. For F-actin quantifications in Kune RNAi images, the ratio between F-actin intensity in *en-Gal4*–positive cells and *en-Gal4*–negative cells was calculated for each embryo.

To measure Nrx-IV, Nrg, and E-cad intensities, maximum Z projections of *Nrx-IV-GFP*, *Nrg-GFP*, and *ubi-E-cad::GFP* stacks were used, respectively. Background fluorescence was subtracted from each image. The *Cherry::Moesin* channel was used to confirm the location of the wound edge. Junctions were outlined using a 4-pixel-wide segmented line and the average intensity obtained using the Measure tool. To calculate the intensity decrease (fold change) at the wound edge, the intensity value for each wound edge junction after wounding (10 and 30 mpw) was divided by the intensity value obtained for the same junction before wounding (Nrx-IV and E-cad), or the intensity value of the whole edge was measured after wounding (10 and 30 mpw) and divided by the intensity value obtained for 10 junctions before wounding (Nrg).

To measure Nrx-IV and Nrg apical ratios, YZ sections were used. Background fluorescence was subtracted from each image. The *Cherry::Moesin* channel was used to confirm apical–basal limits of each cell. The whole apical–basal region was outlined using a 4-pixel-wide segmented line, and the average intensity was obtained using the Measure tool. The same procedure was applied to the apical half of the cell. The intensity at the apical region was calculated as the ratio between the intensity at the apical region and the total intensity for each cell.

Wound area

Maximum Z projections were obtained from *Cherry::Moesin* or *GFP::Moesin* stacks, an ellipse was drawn along the wound edge, and the area was obtained using the Measure tool. For each embryo, the area was normalized relative to the initial wound area.

Cellular protrusions

Maximum Z projections of *Cherry::Moesin* stacks were used, and protrusions were analyzed similar to what has been described (Abreu-Blanco et al., 2012; Zulueta-Coarasa et al., 2014). Briefly, each image was adjusted to an intensity threshold, which was the mean intensity of the image plus one SD. The area inside the wound, adjacent to the actin cable, was outlined with a 2.75-µm-wide line, and the number of pixels were measured and normalized to the total area. For this analysis, control and *kune* mild embryos were considered.

Cell area and aspect ratio

Maximum Z projections of *ubi-E-cad::GFP* images were used. Cells were outlined, and the area and aspect ratio were measured using the Measure tool. The aspect ratio reflects the ratio between the length along the dorsal–ventral and the length along the anterior–posterior axis. Cells were identified by their position relative to sensory organ precursors, which are located in the smooth cell layer 2, two layers anterior to denticle layer 1.

Neighboring cells and exchange events

Maximum Z projections of E-cad::GFP–labeled embryos during the first 45 min after wound closure, acquired with a time interval of 2.5 min, were used. An algorithm based on the invasion percolation of Ranked Surfaces (Schrenk et al., 2012) was devised

to segment cells using GNU Image Manipulation Program (GIMP) and MATLAB (MathWorks), described as follows. First, a point inside the limits of every cell is marked manually. Each of these points is then uniquely identified as a cluster of pixels with a given label such that we have as many clusters as cells. All the nearest neighboring pixels of every cluster are added to a list of pixels and sorted according to their grayscale intensity. The first pixel of the list, the darkest one, is removed from the list and added to the same cluster of the neighboring pixel (meaning that it belongs to the same cell) identified with the proper label. The nearest neighbors of this new pixel that are not yet in the list are then added to the list. We proceeded iteratively in the same way, following the list of pixels sorted by their grayscale intensity until all pixels belonged to one of the clusters (cells). Since the membranes of the cells were the lightest regions, they were the last to be painted, which allowed us to trace the boundaries of the cells. These segmented images were used to quantify the number of cells and neighbors of each cell in the first two rows closer to the wound edge.

For neighbor exchange events, all cells from the first row adjacent to the wound edge were quantified. For each cell, the number of events was measured (gain or loss of neighbors). This value was normalized to the total number of cells in the first row to obtain the ratio of neighbor exchange events for each embryo. To calculate the fraction of cells undergoing neighbor exchange events, the number of cells performing these events was divided by the total number of cells in the first row adjacent to the wound margin. For this analysis, control and *kune* strong mutants were considered.

Displacements upon laser cutting

Single slices of the *ubi–E-cad::GFP* channel were used. A straight line between the two vertices associated with the cut junctions was drawn, and its length was measured using the Measure tool. To model the data, an exponential function was fit to the displacement values over time using the least-square regression method, and values for the time constant (retardation time) and the plateau (maximum displacement) were calculated using Prism (GraphPad Software). To analyze the weak power law behavior of the data, displacement values were log transformed, a linear regression was fit using the least-squares regression method, and values for the slope and intercept were calculated using Prism.

Statistics

Statistical analysis was performed using Prism and Excel (Microsoft). Statistical tests, P values, sample sizes, and error bars are indicated in the respective figure legends.

Theoretical modeling

The simplest possible viscoelastic model that describes our laser cut experiments (Fig. 8) is depicted in Fig. S5 G. The tissue is represented by a regular structure of cells, for which each membrane segment is associated with a KV viscoelastic element composed of a spring of stiffness G and dashpot of drag coefficient η, both in parallel. All cells were initially at rest, and the membranes were under the homeostatic tension F_0. Each membrane segment of equilibrium length x had an initial length $X_0 = x + u_0$. The initial deformation of the membrane was related to the initial tension of the tissue through $u_0 = F_0/G$. If only one membrane was cut, the associated vertices would relax and move slightly toward the interior of their neighboring cells. If the inertia of this system was neglected (small Reynolds number regimen), the sum of the forces applied to each vertex must be 0, which implies $F = 0$ at all times. The deformation of each membrane $u(t)$ (see Fig. S5) may be obtained through the KV constitutive equation $F = Gu + \eta\dot{u} = 0$, where the dot represents a time derivative, and which has the simple solution $u(t) = u_0 e^{-t/\tau}$, with $\tau = \eta/G$ as the retardation time. To simplify our analysis, if we suppose that all other vertices are fixed, the relation between the deformation $u(t)$ of each membrane and the displacement ξ of the vertex is given by geometry. For small deformations, the displacement of the vertices was given by

$$d \propto \frac{F_0}{G}(1 - e^{-t/\tau}). \quad (1)$$

The constant of proportionality varied with the geometry of the cells. As it may be seen from Fig. 8 (A and B), the geometry of the epithelial cells was irregular. To have quantifiable results, we only measured displacements in cells with similar geometries (smooth cells). As it may be seen from Eq. 1, the wound opening time, i.e., the time necessary for the vertices to reach their maximum displacement, was associated with the retardation time of the KV model, $\tau = \eta/G$. The initial displacement velocity is proportional to F_0/η, and the maximum displacement is proportional to F_0/G.

A fit of our data gives us $\tau = 13.9 \pm 2.2$ s and $d_M = 2.74 \pm 0.15$ µm for controls versus $\tau = 9.0 \pm 1.2$ s and $d_M = 2.77 \pm 0.09$ µm for *kune* (Fig. 8 C). These results suggest that even if the tension F_0 and stiffness G are altered in the mutant, their ratio remains approximately constant. However, the smaller retardation time in the mutant can be explained either by a larger stiffness (and consequently a larger tension) or a smaller drag coefficient.

The simple KV model described above includes only the main mechanisms involved in cell and tissue relaxation. To improve our viscoelastic model, each membrane segment may be associated with more complicated viscoelastic elements (Tschoegl, 1989), yielding a better approximation of the experimental displacement of the vertices. A careful inspection of the average displacement for the initial time window ($t < 20$ s) is compatible with the weak power law behavior:

$$d = \frac{F_0}{G'}\left(\frac{t}{\tau'}\right)^{\alpha}, \quad (2)$$

where G' and $\tau' = \eta'/G'$ are scale factors for stiffness and time, and η' a scale factor for the effective drag coefficient of the tissue. The weak power law behavior may be a consequence of not only one but a collection of connected KV elements (in series), with a spectrum of retardation modes with different time scales reflecting for instance the fractal structure of the tissue and the cell's cytoskeleton (Patrício et al., 2015). This power law behavior has been also frequently associated to the soft glassy material model (Sollich et al., 1997) or its extended version, the soft wormlike chain model (Kroy and Glaser, 2007), in which there is a collection of relaxation modes (associated with Maxwell elements; a spring and a dashpot in series) with different time scales, reflect-

ing a glassy behavior. The system was considered to be solidlike whenever $0 < \alpha < 0.5$ and fluidlike whenever $0.5 < \alpha < 1$.

Interestingly, the power law exponents for the WT and *kune* mutant are approximately the same and close to 0.44, revealing systems which have both solid and fluidic behaviors. The higher prefactor, $F_0/(G'^{1-\alpha}\eta'^{\alpha})$, observed for the mutant case may be justified by a larger tension or a smaller effective drag coefficient. In analogous experiments, similar power law exponents (close to 0.4) were obtained for the amnioserosa cell tissues in the fruit fly at different stages of growth (Ma et al., 2009).

Microrheology measurements performed by attaching magnetic microspheres to the cell and applying external oscillatory magnetic fields also revealed the same type of power law behaviors (Fabry et al., 2001). The weak power law exponents, which are associated in this case with the mechanical properties of one individual cell, are smaller (more solidlike), often close to 0.2 for different types of cells, but they may take, in some occasions, higher or lower values (Kollmannsberger and Fabry, 2011; Pritchard et al., 2014).

Online supplemental material

Fig. S1 shows that the mutant *sinu* also develops a wound-closure phenotype. Fig. S2 shows that myosin intensity correlates with wound perimeter over time and that cellular protrusions are not affected in *kune* mutants. Fig. S3 shows Nrg-GFP and Coracle dynamics during wound closure in controls and *kune* mutants. Fig. S4 shows that Coracle is down-regulated in Kune RNAi–expressing cells and that wound-closure phenotypes in Kune RNAi embryos vary depending on wound size. Fig. S5 shows that *kune* mutant and RNAi affect cell shape in a nonautonomous manner and depicts a scheme on the KV model. Video 1 shows wound-closure dynamics in control, *kune* mild, and *kune* strong mutant embryos marked with an F-actin reporter. Video 2 shows Nrx-IV–GFP and F-actin dynamics in a control embryo. Video 3 shows Nrx-IV–GFP and F-actin dynamics in a *kune* strong mutant embryo. Video 4 shows wound-closure dynamics in control and *kune* RNAi minus embryos marked with an F-actin reporter. Video 5 shows wound-closure dynamics in control and *kune* RNAi plus embryos marked with an F-actin reporter. Video 6 shows the response to a laser cut in control and *kune* mutant embryos marked with an E-cad reporter.

Acknowledgments

We are indebted to Nina Matova for her insight and precious contributions; she will be remembered forever. We are grateful to T. Pereira for invaluable support on imaging and data analysis; M. Behrndt and D. Siekhaus for advice and technical help in laser-cutting experiments; C. Crespo and F. Vasconcelos for manuscript review; past and present members of the Tissue Morphogenesis and Repair Lab and R. Teodoro for helpful discussions and technical help; C. Martins for technical help; the microscopy facilities at Chronic Diseases Research Center, Instituto de Medicina Molecular, and Instituto Gulbenkian de Ciencia; the Bloomington Drosophila Stock Center (NIH P40OD018537), the TRiP at Harvard Medical School (NIH/NIGMS R01-GM084947), the Yale School of Medicine Flytrap project, and the Kyoto Stock Center (Drosophila Genomics Resource Center) for providing *Drosophila* lines.

This research was supported by Fundação para a Ciência e a Tecnologia (SFRH/BPD/84569/2012 to L. Carvalho, PD/BD/106058/2015 to S. Ponte, SFRH/BD/119240/2016 to A.S. Nunes, UID/FIS/00618/2013, PTDC/FIS-MAC/28146/2017, PTDC/BIA-BID/29709/2017 and CONGENTO), the European Research Council (2007-StG-208631 and ERC-2015-PoC-713735-EMODI), a European Commission Marie Curie Intra-European Fellowship (PIEF-GA-2009-255573), the Partenariat Hubert Curien Pessoa program (30920XM), the European Science Foundation (Quantitative Models of Cellular and Developmental Biology Research Networking Program, grant 6839), and the iNOVA4Health Research Unit (UID/Multi/04462/2013), cofunded by Fundação para a Ciência e Tecnologia, through national funds and by FED ER under the PT2020 Partnership Agreement.

The authors declare no competing financial interests.

Author contributions: L. Carvalho conceived, conducted, and analyzed all experiments, assembled all figures and videos (except Fig. S5 G), and wrote the paper; P. Patricio performed the theoretical modelling, helped analyzing data in Figs. 7 and 8, assembled Fig. S5 G, and wrote the paper; S. Ponte helped conducting and analyzing experiments in Figs. 1, 2, and S1 and edited the paper; C.P. Heisenberg supervised experiments in Fig. 8 and edited the paper; L. Almeida helped in the theoretical modelling and interpreting the data in Fig. 8; A.S. Nunes and N.A.M. Araújo devised the algorithm for image segmentation and analyzed the number of neighboring cells; A. Jacinto supervised the study, contributed to experimental design, and edited the paper.

Submitted: 10 April 2018
Revised: 15 August 2018
Accepted: 5 September 2018

References

Abreu-Blanco, M.T., J.M. Verboon, R. Liu, J.J. Watts, and S.M. Parkhurst. 2012. Drosophila embryos close epithelial wounds using a combination of cellular protrusions and an actomyosin purse string. *J. Cell Sci.* 125:5984–5997. https://doi.org/10.1242/jcs.109066

Balda, M.S., and K. Matter. 2016. Tight junctions as regulators of tissue remodelling. *Curr. Opin. Cell Biol.* 42:94–101. https://doi.org/10.1016/j.ceb.2016.05.006

Banerjee, S., A.D. Sousa, and M.A. Bhat. 2006. Organization and function of septate junctions: an evolutionary perspective. *Cell Biochem. Biophys.* 46:65–77. https://doi.org/10.1385/CBB:46:1:65

Behrndt, M., G. Salbreux, P. Campinho, R. Hauschild, F. Oswald, J. Roensch, S.W. Grill, and C.-P. Heisenberg. 2012. Forces driving epithelial spreading in zebrafish gastrulation. *Science.* 338:257–260. https://doi.org/10.1126/science.1224143

Brand, A.H., and N. Perrimon. 1993. Targeted gene expression as a means of altering cell fates and generating dominant phenotypes. *Development.* 118:401–415.

Buszczak, M., S. Paterno, D. Lighthouse, J. Bachman, J. Planck, S. Owen, A.D. Skora, T.G. Nystul, B. Ohlstein, A. Allen, et al. 2007. The carnegie protein trap library: a versatile tool for Drosophila developmental studies. *Genetics.* 175:1505–1531. https://doi.org/10.1534/genetics.106.065961

Campàs, O. 2016. A toolbox to explore the mechanics of living embryonic tissues. *Semin. Cell Dev. Biol.* 55:119–130. https://doi.org/10.1016/j.semcdb.2016.03.011

Campos, I., J.A. Geiger, A.C. Santos, V. Carlos, and A. Jacinto. 2010. Genetic screen in Drosophila melanogaster uncovers a novel set of genes re-

quired for embryonic epithelial repair. *Genetics.* 184:129–140. https://doi.org/10.1534/genetics.109.110288

Carvalho, L., A. Jacinto, and N. Matova. 2014. The Toll/NF-κB signaling pathway is required for epidermal wound repair in Drosophila. *Proc. Natl. Acad. Sci. USA.* 111:E5373–E5382. https://doi.org/10.1073/pnas.1408224111

Choi, W., B.R. Acharya, G. Peyret, M.A. Fardin, R.M. Mège, B. Ladoux, A.S. Yap, A.S. Fanning, and M. Peifer. 2016. Remodeling the zonula adherens in response to tension and the role of afadin in this response. *J. Cell Biol.* 213:243–260.

Dubreuil, R.R. 2006. Functional links between membrane transport and the spectrin cytoskeleton. *J. Membr. Biol.* 211:151–161. https://doi.org/10.1007/s00232-006-0863-y

Ducuing, A., and S. Vincent. 2016. The actin cable is dispensable in directing dorsal closure dynamics but neutralizes mechanical stress to prevent scarring in the Drosophila embryo. *Nat. Cell Biol.* 18:1149–1160. https://doi.org/10.1038/ncb3421

Fabry, B., G.N. Maksym, J.P. Butler, M. Glogauer, D. Navajas, and J.J. Fredberg. 2001. Scaling the microrheology of living cells. *Phys. Rev. Lett.* 87:148102. https://doi.org/10.1103/PhysRevLett.87.148102

Fanning, A.S., C.M. Van Itallie, and J.M. Anderson. 2012. Zonula occludens-1 and -2 regulate apical cell structure and the zonula adherens cytoskeleton in polarized epithelia. *Mol. Biol. Cell.* 23:577–590. https://doi.org/10.1091/mbc.e11-09-0791

Fernandez-Gonzalez, R., and J.A. Zallen. 2013. Wounded cells drive rapid epidermal repair in the early Drosophila embryo. *Mol. Biol. Cell.* 24:3227–3237. https://doi.org/10.1091/mbc.e13-05-0228

Fernandez-Gonzalez, R., S. de M. Simoes, J.C. Röper, S. Eaton, and J.A. Zallen. 2009. Myosin II dynamics are regulated by tension in intercalating cells. *Dev. Cell.* 17:736–743. https://doi.org/10.1016/j.devcel.2009.09.003

Garcia-Fernandez, B., I. Campos, J. Geiger, A.C. Santos, and A. Jacinto. 2009. Epithelial resealing. *Int. J. Dev. Biol.* 53:1549–1556. https://doi.org/10.1387/ijdb.072308bg

Geiger, J.A., L. Carvalho, I. Campos, A.C. Santos, and A. Jacinto. 2011. Hole-in-one mutant phenotypes link EGFR/ERK signaling to epithelial tissue repair in Drosophila. *PLoS One.* 6:e28349. https://doi.org/10.1371/journal.pone.0028349

Halfon, M.S., S. Gisselbrecht, J. Lu, B. Estrada, H. Keshishian, and A.M. Michelson. 2002. New fluorescent protein reporters for use with the Drosophila Gal4 expression system and for vital detection of balancer chromosomes. *Genesis.* 34:135–138. https://doi.org/10.1002/gene.10136

Hall, S., and R.E. Ward IV. 2016. Septate junction proteins play essential roles in morphogenesis throughout embryonic development in Drosophila. *G3 (Bethesda).* 6:2375–2384. https://doi.org/10.1534/g3.116.031427

Harden, N., S.J.H. Wang, and C. Krieger. 2016. Making the connection - shared molecular machinery and evolutionary links underlie the formation and plasticity of occluding junctions and synapses. *J. Cell Sci.* 129:3067–3076. https://doi.org/10.1242/jcs.186627

Harris, T.J.C., and U. Tepass. 2010. Adherens junctions: from molecules to morphogenesis. *Nat. Rev. Mol. Cell Biol.* 11:502–514. https://doi.org/10.1038/nrm2927

Hatte, G., C. Prigent, and J.-P. Tassan. 2018. Tight junctions negatively regulate mechanical forces applied to adherens junctions in vertebrate epithelial tissue. *J. Cell Sci.* 131:jcs208736. https://doi.org/10.1242/jcs.208736

Huang, J., W. Zhou, W. Dong, A.M. Watson, and Y. Hong. 2009. From the Cover: Directed, efficient, and versatile modifications of the Drosophila genome by genomic engineering. *Proc. Natl. Acad. Sci. USA.* 106:8284–8289. https://doi.org/10.1073/pnas.0900641106

Hunter, M.V., D.M. Lee, T.J.C. Harris, and R. Fernandez-Gonzalez. 2015. Polarized E-cadherin endocytosis directs actomyosin remodeling during embryonic wound repair. *J. Cell Biol.* 210:801–816. https://doi.org/10.1083/jcb.201501076

Jonusaite, S., A. Donini, and S.P. Kelly. 2016. Occluding junctions of invertebrate epithelia. *J. Comp. Physiol. B.* 186:17–43. https://doi.org/10.1007/s00360-015-0937-1

Kiehart, D.P., C.G. Galbraith, K.A. Edwards, W.L. Rickoll, and R.A. Montague. 2000. Multiple forces contribute to cell sheet morphogenesis for dorsal closure in Drosophila. *J. Cell Biol.* 149:471–490. https://doi.org/10.1083/jcb.149.2.471

Kollmannsberger, P., and B. Fabry. 2011. Linear and Nonlinear Rheology of Living Cells. *Annu. Rev. Mater. Res.* 41:75–97. https://doi.org/10.1146/annurev-matsci-062910-100351

Krieg, M., A.R. Dunn, and M.B. Goodman. 2014. Mechanical control of the sense of touch by β-spectrin. *Nat. Cell Biol.* 16:224–233. https://doi.org/10.1038/ncb2915

Kroy, K., and J. Glaser. 2007. The glassy wormlike chain. *New J. Phys.* 9:416. https://doi.org/10.1088/1367-2630/9/11/416

Laval, M., C. Bel, and C. Faivre-Sarrailh. 2008. The lateral mobility of cell adhesion molecules is highly restricted at septate junctions in Drosophila. *BMC Cell Biol.* 9:38. https://doi.org/10.1186/1471-2121-9-38

Lye, C.M., H.W. Naylor, and B. Sanson. 2014. Subcellular localisations of the CPTI collection of YFP-tagged proteins in Drosophila embryos. *Development.* 141:4006–4017. https://doi.org/10.1242/dev.111310

Ma, X., H.E. Lynch, P.C. Scully, and M.S. Hutson. 2009. Probing embryonic tissue mechanics with laser hole drilling. *Phys. Biol.* 6:036004. https://doi.org/10.1088/1478-3975/6/3/036004

Matsubayashi, Y., C.C. Gilmer, and T.H. Millard. 2015. Endocytosis-dependent coordination of multiple actin regulators is required for wound healing. *J. Cell Biol.* 210:419–433.

Mayer, M., M. Depken, J.S. Bois, F. Jülicher, and S.W. Grill. 2010. Anisotropies in cortical tension reveal the physical basis of polarizing cortical flows. *Nature.* 467:617–621. https://doi.org/10.1038/nature09376

Meng, F., and F. Sachs. 2012. Orientation-based FRET sensor for real-time imaging of cellular forces. *J. Cell Sci.* 125:743–750. https://doi.org/10.1242/jcs.093104

Millard, T.H., and P. Martin. 2008. Dynamic analysis of filopodial interactions during the zippering phase of Drosophila dorsal closure. *Development.* 135:621–626. https://doi.org/10.1242/dev.014001

Morin, X., R. Daneman, M. Zavortink, and W. Chia. 2001. A protein trap strategy to detect GFP-tagged proteins expressed from their endogenous loci in Drosophila. *Proc. Natl. Acad. Sci. USA.* 98:15050–15055. https://doi.org/10.1073/pnas.261408198

Nelson, K.S., M. Furuse, and G.J. Beitel. 2010. The Drosophila Claudin Kunekune is required for septate junction organization and tracheal tube size control. *Genetics.* 185:831–839. https://doi.org/10.1534/genetics.110.114959

Oda, H., and S. Tsukita. 1999. Nonchordate classic cadherins have a structurally and functionally unique domain that is absent from chordate classic cadherins. *Dev. Biol.* 216:406–422. https://doi.org/10.1006/dbio.1999.9494

Oshima, K., and R.G. Fehon. 2011. Analysis of protein dynamics within the septate junction reveals a highly stable core protein complex that does not include the basolateral polarity protein Discs large. *J. Cell Sci.* 124:2861–2871. https://doi.org/10.1242/jcs.087700

Paluch, E., and C.-P. Heisenberg. 2009. Biology and physics of cell shape changes in development. *Curr. Biol.* 19:R790–R799. https://doi.org/10.1016/j.cub.2009.07.029

Patrício, P., C.R. Leal, J. Duarte, and C. Januário. 2015. Rheology of the cytoskeleton as a fractal network. *Phys. Rev. E Stat. Nonlin. Soft Matter Phys.* 92:040702. https://doi.org/10.1103/PhysRevE.92.040702

Price, M.H., D.M. Roberts, B.M. McCartney, E. Jezuit, and M. Peifer. 2006. Cytoskeletal dynamics and cell signaling during planar polarity establishment in the Drosophila embryonic denticle. *J. Cell Sci.* 119:403–415. https://doi.org/10.1242/jcs.02761

Pritchard, R.H., Y.Y. Huang, and E.M. Terentjev. 2014. Mechanics of biological networks: from the cell cytoskeleton to connective tissue. *Soft Matter.* 10:1864–1884. https://doi.org/10.1039/c3sm52769g

Razzell, W., W. Wood, and P. Martin. 2014. Recapitulation of morphogenetic cell shape changes enables wound re-epithelialisation. *Development.* 141:1814–1820. https://doi.org/10.1242/dev.107045

Schindelin, J., I. Arganda-Carreras, E. Frise, V. Kaynig, M. Longair, T. Pietzsch, S. Preibisch, C. Rueden, S. Saalfeld, B. Schmid, et al. 2012. Fiji: an open-source platform for biological-image analysis. *Nat. Methods.* 9:676–682. https://doi.org/10.1038/nmeth.2019

Schrenk, K.J., N.A.M. Araújo, J.S. Andrade Jr., and H.J. Herrmann. 2012. Fracturing ranked surfaces. *Sci. Rep.* 2:348. https://doi.org/10.1038/srep00348

Sens, K.L., S. Zhang, P. Jin, R. Duan, G. Zhang, F. Luo, L. Parachini, and E.H. Chen. 2010. An invasive podosome-like structure promotes fusion pore formation during myoblast fusion. *J. Cell Biol.* 191:1013–1027. https://doi.org/10.1083/jcb.201006006

Shen, L. 2012. Tight junctions on the move: molecular mechanisms for epithelial barrier regulation. *Ann. N. Y. Acad. Sci.* 1258:9–18. https://doi.org/10.1111/j.1749-6632.2012.06613.x

Simone, R.P., and S. DiNardo. 2010. Actomyosin contractility and Discs large contribute to junctional conversion in guiding cell alignment within the Drosophila embryonic epithelium. *Development.* 137:1385–1394. https://doi.org/10.1242/dev.048520

Sluysmans, S., E. Vasileva, D. Spadaro, J. Shah, F. Rouaud, and S. Citi. 2017. The role of apical cell-cell junctions and associated cytoskeleton in

mechanotransduction. *Biol. Cell.* 109:139–161. https://doi.org/10.1111/boc.201600075

Sollich, P., F. Lequeux, P. Hébraud, and M.E. Cates. 1997. Rheology of soft glassy materials. *Phys. Rev. Lett.* 78:2020–2023. https://doi.org/10.1103/PhysRevLett.78.2020

St Johnston, D. 2013. Using mutants, knockdowns, and transgenesis to investigate gene function in Drosophila. *Wiley Interdiscip. Rev. Dev. Biol.* 2:587–613. https://doi.org/10.1002/wdev.101

Tornavaca, O., M. Chia, N. Dufton, L.O. Almagro, D.E. Conway, A.M. Randi, M.A. Schwartz, K. Matter, and M.S. Balda. 2015. ZO-1 controls endothelial adherens junctions, cell-cell tension, angiogenesis, and barrier formation. *J. Cell Biol.* 208:821–838. https://doi.org/10.1083/jcb.201404140

Tschoegl, N.W. 1989. The Phenomenological theory of linear viscoelastic behavior. An introduction. Springer-Verlag Berlin and Heidelberg GmbH and Co.https://doi.org/10.1007/978-3-642-73602-5

Tsoumpekos, G., L. Nemetschke, and E. Knust. 2018. Drosophila Big bang regulates the apical cytocortex and wing growth through junctional tension. *J. Cell Biol.* 217:1033. https://doi.org/10.1083/jcb.201705104

Volksdorf, T., J. Heilmann, S.A. Eming, K. Schawjinski, M. Zorn-Kruppa, C. Ueck, S. Vidal-Y-Sy, S. Windhorst, M. Jücker, I. Moll, and J.M. Brandner. 2017. Tight Junction Proteins Claudin-1 and Occludin Are Important for Cutaneous Wound Healing. *Am. J. Pathol.* 187:1301–1312. https://doi.org/10.1016/j.ajpath.2017.02.006

Walters, J.W., S.A. Dilks, and S. DiNardo. 2006. Planar polarization of the denticle field in the Drosophila embryo: roles for Myosin II (zipper) and fringe. *Dev. Biol.* 297:323–339. https://doi.org/10.1016/j.ydbio.2006.04.454

Wood, W., A. Jacinto, R. Grose, S. Woolner, J. Gale, C. Wilson, and P. Martin. 2002. Wound healing recapitulates morphogenesis in Drosophila embryos. *Nat. Cell Biol.* 4:907–912. https://doi.org/10.1038/ncb875

Wu, V.M., and G.J. Beitel. 2004. A junctional problem of apical proportions: epithelial tube-size control by septate junctions in the Drosophila tracheal system. *Curr. Opin. Cell Biol.* 16:493–499. https://doi.org/10.1016/j.ceb.2004.07.008

Zulueta-Coarasa, T., and R. Fernandez-Gonzalez. 2017. Tension (re)builds: Biophysical mechanisms of embryonic wound repair. *Mech. Dev.* 144(Pt A):43–52. https://doi.org/10.1016/j.mod.2016.11.004

Zulueta-Coarasa, T., M. Tamada, E.J. Lee, and R. Fernandez-Gonzalez. 2014. Automated multidimensional image analysis reveals a role for Abl in embryonic wound repair. *Development.* 141:2901–2911. https://doi.org/10.1242/dev.106898